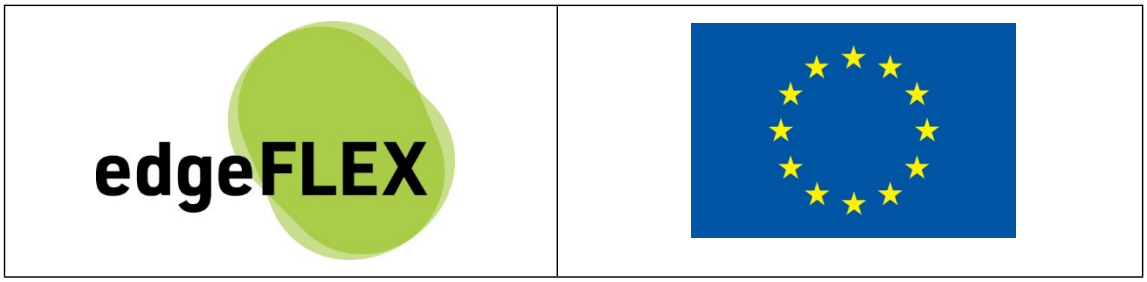

edgeFLEX

D2.2 v1.0

Frequency Control Concepts for Current VPPs in Large Scale Deployment

The research leading to these results has received funding from the European Union's Horizon 2020 Research and Innovation Programme, under Grant Agreement no 883710.

Project Name:	edgeFLEX
Contractual Delivery Date:	31.03.2021
Actual Delivery Date:	31.03.2021
Authors:	Georgios Tzounas (UCD), Junru Chen (UCD), Taulant Kërçi (UCD), Weilin Zhong (UCD), Federico Milano (UCD)
Workpackage:	WP2 – Frequency and Inertia Response Control Concept for Dynamically Controlled VPP Solutions
Security:	P
Nature:	R
Version:	V1.0
Total number of pages:	62

Abstract

This deliverable describes frequency control and metering strategies for virtual power plants connected at the transmission and/or distribution voltage levels. These include coordinated control strategies for both primary and secondary frequency control, a measurement-based technique to estimate the amount of frequency regulation provided by grid-connected devices, as well as an online inertia estimation method that can be utilized to improve the fast frequency response of virtual power plants. All algorithms are tested through computer-based simulations according to the relevant scenarios defined in deliverable D2.1.

Keyword list

Frequency control, virtual power plants, distributed energy resources, converter-interfaced generation, energy storage systems, power system dynamics, inertia estimation, phasor measurement units.

Disclaimer

All information provided reflects the status of the edgeFLEX project at the time of writing and may be subject to change.

Executive Summary

This deliverable, which is the major output of task T2.2 in the work package WP2 of edgeFLEX, describes the frequency control concepts and algorithms developed for Virtual Power Plants (VPPs) in large scale deployment. These include coordinated control strategies for both Primary Frequency Control (PFC) and Secondary Frequency Control (SFC), a measurement-based technique to estimate the amount of frequency regulation provided by grid-connected devices, as well as an online inertia estimation method that can be utilized to improve the VPP Fast Frequency Response (FFR). The algorithms are tested through computer-based simulations according to the relevant scenarios defined in deliverable D2.1.

The control strategy adopted for the provision of PFC is an important relevant aspect of VPP regulation. The deliverable presents a centralized, coordinated frequency control strategy for the Distributed Energy Resources (DERs) that compose a VPP, and studies the effect of such strategy on the overall short-term dynamic behavior considering both deterministic and stochastic simulations. The impact of communication network-induced delays on the VPP dynamic response is also discussed and evaluated.

Another relevant aspect for Transmission System Operators (TSOs) is the impact of a linear aggregate operation of the DERs that compose a VPP on the dynamic response of the transmission system. With this regard, the deliverable considers an Automatic Generation Control (AGC) approach to operate and coordinate the DERs that compose the VPP. For the sake of comparison, the performance of the AGC-based VPP is compared to a method that optimally schedules the DERs that compose the VPP based on the solution of a Mixed-Integer Linear Programming (MILP) problem. The MILP is embedded into a time domain simulator by means of a co-simulation framework The AGC-based approach is shown to lead to a better dynamic performance of the system as compared to that of the MILP-based VPPs scheduling.

The deliverable also presents a technique to estimate the rate of change of regulated power of any given grid-connected device. The novelty of this technique is that it defines a local index that is able to discriminate between devices that modify the frequency at the connection bus and devices that do not. A significant contribution of this deliverable is, hence, that it discusses how to determine whether a device connected to the grid is providing inertial response and/or frequency control. A taxonomy of devices based on their ability to modify locally the frequency is proposed. The properties of the proposed index are illustrated through examples based on the Synchronous Machine (SM) and its controllers, as well as on non-synchronous devices, namely, passive loads, Energy Storage Systems (ESSs), and Thermostatically-Controlled Loads (TCLs). Finally, a statistical approach is presented to evaluate the inertial response and fast frequency regulation provided by non-synchronous devices, such as Wind Power Plants (WPPs).

A byproduct of the aforementioned index is a method to estimate on-line the inertia of synchronous machines as well as track the equivalent inertia of non-synchronous monitored devices during transient conditions. Relevant numerical aspects of the method are also duly discussed. For power electronic-based devices, the droop gain of the FFR is also determined as a byproduct of the inertia estimation. The proposed method is shown to be robust against noise and to track accurately the inertia of SMs, Virtual Synchronous Machines (VSMs) with constant and adaptive inertia, and WPPs with inclusion of energy storage-based frequency control.

Authors

Partner	Name	e-mail
UCD		
	Georgios Tzounas	georgios.tzounas@ucdconnect.ie
	Junru Chen	junru.chen.1@ucdconnect.ie
	Taulant Këerçi	taulant.kerci@ucdconnect.ie
	Weilin Zhong	weilin.zhong@ucdconnect.ie
	Federico Milano	federico.milano@ucd.ie

Table of Contents

1. Introduction

1.1 Task 2.2

This deliverable is the major output of task T2.2 in the work package WP2. The main goal of T2.2 is to review the current trends in frequency control of DERs, such as WPPs and Solar Photovoltaics (SPVs) and the coordination with ESSs. The vast majority of the work carried out in this topic are based on optimisation techniques and centralised control approaches. The most promising approaches to be implemented in real-time are identified and tested considering the scenarios identified in Task 2.1.

1.2 Objectives and Outline of the Deliverable

This deliverable aims at describing the frequency control algorithms developed for current VPPs in large scale deployment. A novel control strategy to provide PFC of VPPs in a coordinated way is presented first. Then, a promising AGC approach is described that helps restore the grid frequency to the nominal value and keeps the VPP power injection at the scheduled value. A practical criterion to distinguish between devices that modify the frequency from those who do not based on their Rate of Change of Power (RoCoP) is also provided. The criterion can be utilized to reward ancillary services of grid-connected devices that provide PFC. Finally, based on such criterion, a novel on-line technique to estimate the equivalent inertia and quantify the inertial response provided by non-synchronous devices is presented.

1.3 How to Read this Document

The frequency control concepts presented in this deliverable are tested based on the relevant scenarios and using the data and component models provided in deliverable D2.1. We thus encourage the reader to go through this document while referring in parallel to the material presented in D2.1 whenever relevant. Moreover, the techniques presented in Chapters 2, 3 and 4 of this deliverable have been dropped as containerised software modules to WP4 for integration in the edgeFLEX platform in the context of tasks T4.1-T4.3. Dependencies and links of task T2.2 with other tasks within WP2, as well as of WP2 with other work packages from the edgeFLEX project are summarized in Figure 1.

1.4 Structure of the Deliverable

The remainder of this deliverable is organized as follows. Chapter 2 describes a centralized, coordinated primary frequency regulation strategy for the DERs that compose a VPP. Chapter 3 proposes an AGC approach to coordinate the DERs included in the VPP for the provision of secondary frequency regulation. Chapter 4 provides a practical criterion to determine whether a grid-connected device provides frequency control and/or inertial response. Chapter 5 proposes an on-line method to estimate the inertia of SMs as well as to track the equivalent inertia of converter-interfaced generators. Finally, the deliverable is summarized and conclusions are duly drawn in Chapter 6.

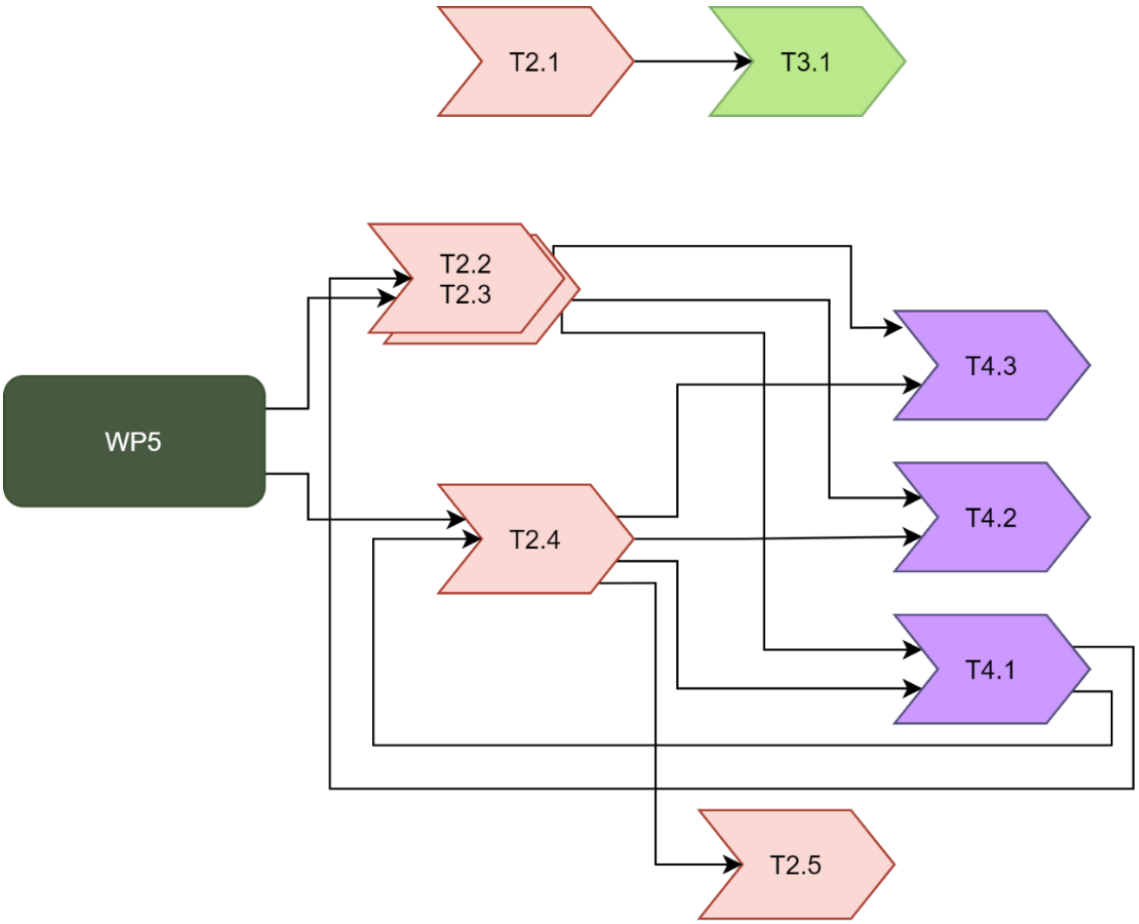

Figure 1 – Relations between WP2 and other work packages

2. Coordinated Primary Frequency Control of VPPs

2.1 Introduction

The primary purpose of a VPP is to optimize the performance of its constituent parts by coordinating the production and consumption [1]. For operation purposes, the active power output of a VPP is scheduled similarly to conventional generators, e.g. through the solution of a daily-ahead unit-commitment problem [2]. In transient conditions, e.g. following a contingency, VPPs have to provide frequency support [3]. The active power scheduling and the frequency control of VPPs are generally decoupled due to their different time scales. Instead, in this chapter these functions are combined by switching to coordinated control of the DERs and ESSs that form the VPP during the contingency [4].

The proposed coordinated VPP frequency control method has been dropped to WP4 as containerized software code and integrated into the edgeFLEX platform, in the context of the relation of WP2 with tasks T4.1-T4.3 of WP4.

2.2 Formulation

The coordinated VPP frequency control method for short-term frequency regulation presented in this section is based on the frequency control technologies discussed in [5]. The diagram of the proposed control strategy is shown in Figure 2. The control structure is similar to a conventional SFC. However, it is aimed at improving the fast frequency response of the VPP and, thus, it operates in the same time scale as the PFC.

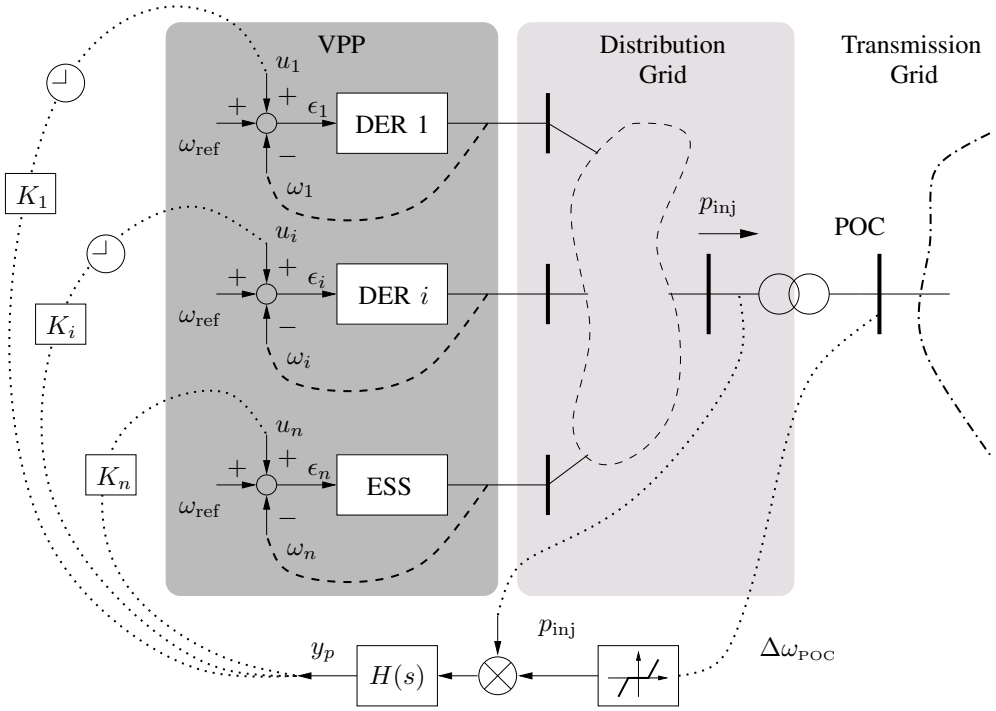

Figure 2 – Control diagram of the proposed coordinated control of VPPs

It is assumed that, in normal operating conditions and in a given period, the VPP power set-point is defined by the TSO based on the solution of an electricity market problem such as the unit commitment. Hence, before the occurrence of any contingency, the active power injection (p_{inj}) is the set-point of the VPP as scheduled by the TSO.

The proposed approach consists in measuring the total active power injected (p_{inj}) into the trans-

mission grid by the VPP as well as the frequency variation ($\Delta\omega_{\mathrm{POC}}$) and then transmitting to the DERs and ESSs that compose the VPP the following signal [4]:

$$y_p = H(s)\,\Delta\omega_{\mathrm{POC}}\,p_{\mathrm{inj}}\,, \tag{2.1}$$

where $H(s)$ is the transfer function of the coordinated control. $H(s)$ includes a proper gain that adjusts the magnitude of y_p and makes it consistent and compatible with the primary frequency controllers of the VPP resources. Apart from a proportional controller, other controllers such as Proportional-Integral (PI) and Low-Pass Filter (LPF) can also be utilized to implement $H(s)$. The case study discussed in Section A.1 of the ANNEX compares and discusses the performance of different controllers.

The rationale of the proposed coordinated control scheme is as follows. In steady-state conditions, the frequency deviation at the Point of Connection (POC) $\Delta\omega_{\mathrm{POC}}$ is zero and hence the primary controllers of the resources that form the VPP are decoupled. For practical implementation issues, a small dead-band is then included in $\Delta\omega_{\mathrm{POC}}$, to avoid unnecessary communications of the control signal y_p when the frequency deviations are negligible. The dead-band is utilized only to make the coordinated control insensitive to noise.

After the occurrence of a major contingency in the transmission grid, e.g. a fault or the outage of a large load/generator, the frequency of the system varies. This events leads to $\Delta\omega_{\mathrm{POC}} \neq 0$ and thus triggers the coordinated feedback control.

The effect of y_p is, in turn, to "amplify" the sensitivity of the primary control with respect to the local frequency deviation by a coefficient that is proportional to the power generated by the VPP. In fact, assuming that $\Delta\omega_{\mathrm{POC}}$ measured at the POC is the same as the local frequency deviation measured by the DERs, one has that the overall signal entering into the primary frequency controllers is:

$$\epsilon_i = (\omega_{\mathrm{ref}} - \omega_i) + u_i \approx [1 + K_i H(s)\,p_{\mathrm{inj}}]\,\Delta\omega_{\mathrm{POC}}\,, \tag{2.2}$$

where $\omega_{\mathrm{ref}} - \omega_i$ is the local frequency error as measured by the ESS or DER controller; and $u_i = K_i y_p$.

Figure 2 shows that timers are included in the signals sent to the DERs. These timers are triggered by a threshold value of u_i and allow improving the coordination of the DERs and ESSs. This point is duly discussed and illustrated in the case study presented in Section A.1 of the ANNEX.

2.3 VPP Control Modes

Six different coordinated control modes are considered for the ESS and DERs in the VPP, as follows.

Mode 1 DERs and ESSs regulate the frequency but are fully independent ($y_p = 0$).

Mode 2 Only the ESS regulates the frequency. DERs do not include a frequency controller. Thus, no coordination is applied in this control mode.

Mode 3 DERs do not include frequency control. The ESS is regulated in order to keep constant the power injection p_{inj} of the VPP at the POC. This is a typical VPP operation mode, where the TSO schedules the VPP output every 15 minutes. Thus, there is no coordination in this control mode.

Mode 4 Weather-driven DERs such as Wind Turbines (WTs) and SPVs are considered non-dispatchable resources due to the stochastic nature of the wind and clouds [1]. The ESS is the only device that regulates the frequency. Therefore, in this mode, only the ESS is fed with the signal y_p.

Mode 5 In [6], it is proposed that wind farms and VPPs can be used for emergency frequency control in smart super grids. Hence, in this mode, both ESS and DERs are coordinated with the signal y_p.

Mode 6 Similarly to Mode 5, both the ESS and DERs are coordinated in this mode. However, the feedback signal y_p is utilized differently for ESS and DERs. The ESS is always fed with y_p and, thus, its primary frequency regulation acts immediately after the contingency. On the other hand, DERs are included in the coordinated control and receive the signal y_p after a given time following the occurrence of the contingency, e.g. 15 s. The timer that activates the feedback signal for the DERs is triggered by the magnitude of the variation of the frequency $\Delta\omega_{\text{POC}}$.

2.4 Simulation Results

The presented coordinated VPP frequency control method is tested by considering Use Case FC_B.1 described in D2.1 and the Key Performance Indicators (KPIs) defined therein. In particular, the load connected to bus 6 in the original Western Systems Coordinating Council (WSCC) system is replaced by a VPP. The VPP is integrated in an 8-bus, 38 kV distribution network [7]. The modified WSCC system with inclusion of the VPP is depicted in Figure 3.

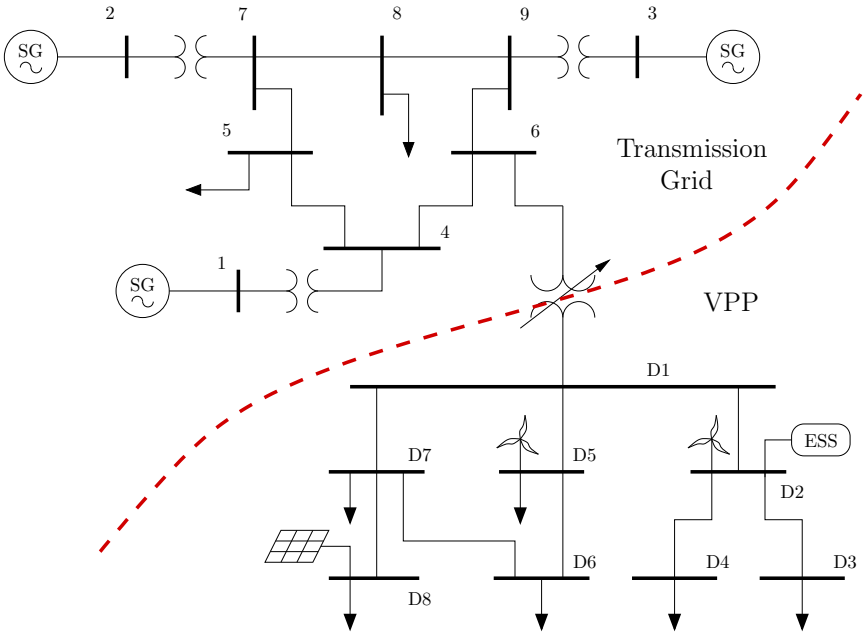

Figure 3 – Modified WSCC system with a VPP connected to bus 6

The structure of the VPP can be described as follows.

- The VPP is connected to the transmission system through an automatic Under-Load Tap Changer (ULTC) type step down transformer.
- A SPV plant, 2 WPPs, and an ESS are connected to buses D8, D5, D2, and D2, respectively, of the distribution network. The dynamic model used to represent the frequency control structure of each non-synchronous device is described in the ANNEX of D2.1. Moreover, the ANNEX of D2.1 also describes the stochastic models used to represent the solar irradiance, the wind speed and the voltage dependence of loads.
- For the purpose of the frequency control, each DER utilizes the frequency signal obtained using a Synchronous Reference Frame Phase-Locked Loop (SRF-PLL) installed at bus D1. The dynamic model used to represent the SRF-PLL is presented in the ANNEX of D2.1. The frequency signal obtained with the SRF-PLL is transmitted to the DERs that compose the VPP. The model employed to represent communication network induced phenomena is described in the ANNEX of D2.1.

- The initial active power generation of the wind power plants and the SPV plant are 15 MW each, while the power rate of the ESS is 10 MW. The initial total active and reactive power consumption of loads in the VPP is 57.8 MW and 11.7 MVar, respectively.
- The focus is on the short-term transient behavior of the power system (few tens of seconds), and thus the impact of the state of charge of the ESS is neglected.

The power injected by the VPP into the grid, namely p_{inj}, is the power flow from bus D1 to bus 6.

Simulation results are presented in in Section A.1 of the ANNEX. Simulations are carried out using the co-simulation software tool described in [8] that combines the Python-based power system simulator Dome [9] and the communication network simulator ns-3 [10].

3. Automatic Generation Control of VPPs

3.1 Introduction

The large-scale integration of DERs into power systems allows more electricity generation from Renewable Energy Sources (RESs) as well as reduces the impact on the environment [11]. However, the penetration of DERs creates additional challenges for TSOs mainly due to their uncertain and variable nature as well as the lack of visibility (i.e., mostly connected on the distribution level) [12]. For this reason, it is important to manage DERs in order to better contribute to electricity markets [13], and system operation [11].

A way to address this problem is to make use of the VPP concept. For example, in the Irish power system, there are many DERs units that operate as a VPP in the electricity market [14]. EirGrid, the Irish TSO, requires that the power output of a VPP increases linearly during the ramp-up time [15]. The TSO does not reward the excess power if the VPP generates more than the agreed linear ramp. On the other hand, the VPP incurs a fine if it is unable to provide the scheduled power [16]. Providing the scheduled power is a challenge for VPPs as different generators have different characteristics (e.g., different capacity, response and ramping time), and thus the aggregate ramping rate may be non-linear.

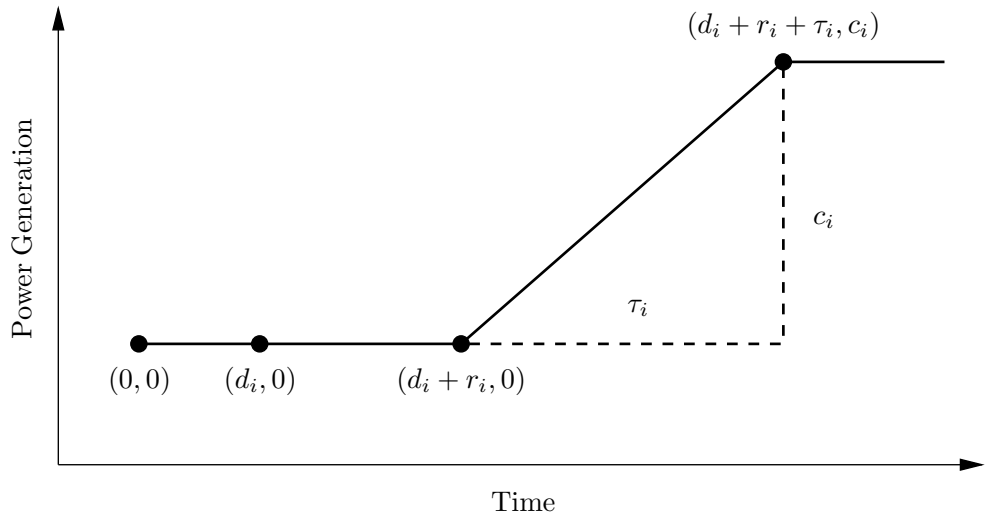

Figure 4 – Power production of a single small generator

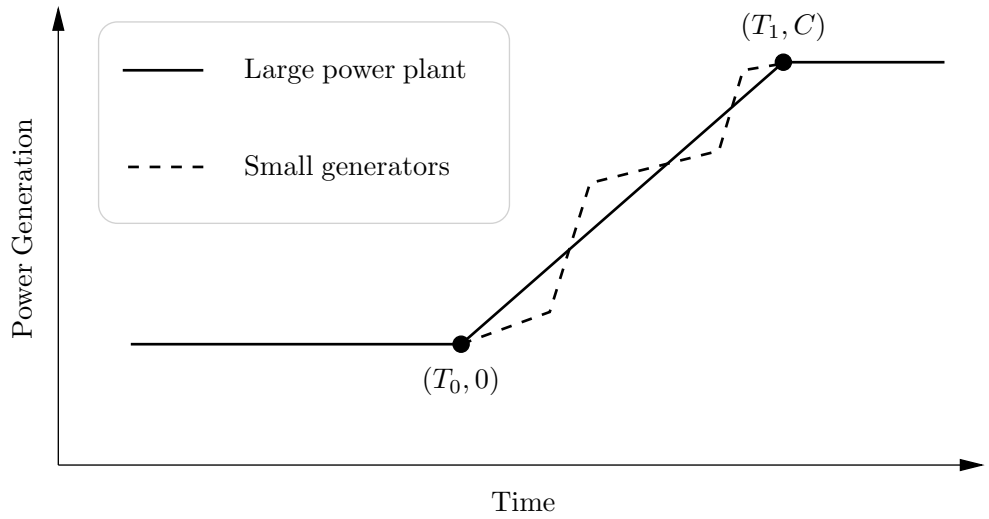

Figure 5 – Power production of a large power plant and of a collection of small generators

To illustrate the problem faced by the VPPs, Figures 4 and 5 show the power production of a single small generator, and the power production of both a single large power plant and that of many small generators, respectively [16]. The points in Figure 4 have the following meanings:

- $(0, 0)$, is the time when the TSO tells the VPP to go to the maximum production.
- $(d_i, 0)$, is an inherent time delay representing how long the VPP takes to send a signal to the i-th generator to start the production.
- $(d_i + r_i, 0)$, is the time at which the i-th generator transitions from the minimum to the ramping production, and r_i is the response time of the i-th generator of the VPP, i.e. how long this generator takes to respond to the instruction from the VPP.
- $(d_i + r_i + \tau_i, c_i)$, is the time at which the i-th generator of the VPP transitions from the ramping to the maximum production, where τ_i is the ramping time and c_i corresponds to the maximum capacity of the i-th generator.

In Figure 5, the solid and dashed lines represent the power generated by a single large power plant (linear), and the total power output of small generators of the VPP (piecewise linear), respectively. A thorough discussion on how to achieve an aggregate ramping rate of the VPP which is as close to linear as possible is given in [16]. The points in Figure 5 have the following meanings:

- $(T_0, 0)$, is the time when the ramping of the VPP begins.
- (T_1, C), is the time when the ramping of the VPP stops, where C corresponds to the total capacity of the generators that compose the VPP.

Motivated by the discussion above, we address the following research questions: (i) what is the impact of linear aggregate response of a VPP on high voltage transmission grid? (ii) is there any difference between imposing or not imposing such a linear ramping response? and what is the best operation and control of a VPP from the TSO point of view?

To answers these questions, an approach based on AGC is proposed in this chapter and used to coordinate the DERs that form the VPP [17]. The AGC approach is compared with an optimization problem based on MILP that optimally schedules the small generators of the VPP in order to achieve a linear ramping.

The proposed AGC approach has been dropped to WP4 as containerized software code and has been integrated into the edgeFLEX platform, in the context of the relation of WP2 with tasks T4.1-T4.3 of WP4.

3.2 Formulation

TSOs rely on SFC to restore the frequency to the nominal value as well as keep the interchange between different areas at the scheduled values [18]. SFC is commonly provided through an AGC scheme that operates in the time scale of tens of seconds up to tens of minutes and eliminates the steady-state frequency error that remains after the PFC [19]. In a standard AGC scheme for SMs, the error between the reference frequency and the measured frequency at a pilot bus is calculated and fed to a controller that eliminates the steady state error [18]. The generated control signal is then distributed by the AGC to the Turbine Governors (TGs) of SMs proportionally to the values of their droops.

In this section, we consider an AGC scheme that coordinates the DERs that compose a VPP. The control scheme of the AGC is shown in Figure 6. The signal $p_{\mathrm{VPP}}^{\mathrm{ref}}$ represents the reference power signal sent by the TSO to the VPP, whereas p_{VPP} represents the sum of the measured active power of the DERs included in the VPP. The AGC includes an integrator with gain K_0 that nullifies the active power steady-state error. The output of the integrator is then distributed to the VPP DER frequency controllers proportionally to their droops $\mathcal{R}_i$.

For the sake of comparison, the frequency variations obtained using the proposed AGC-based VPP are compared to VPP scheduling based on the solution of an optimization problem. To this aim,

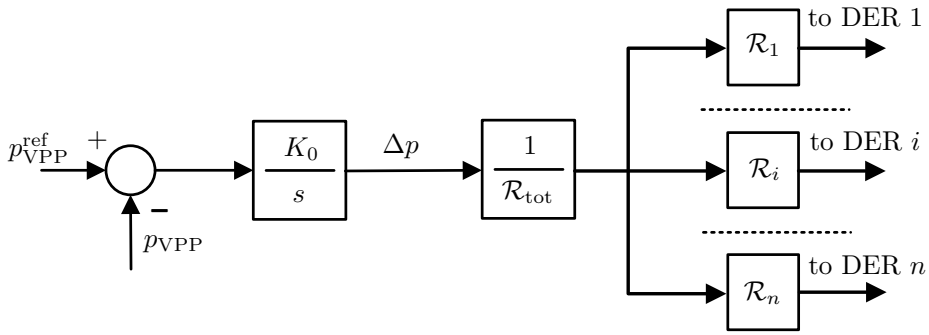

Figure 6 – Basic AGC control scheme for active power regulation of VPPs

we employ the MILP model proposed in [16] to optimally schedule the resources that compose the VPP and obtain a ramping rate that is as close to linear as possible. The improvements of the efficiency and robustness of MILP solvers in recent years have been significant [20] and thus MILP is currently commonly utilized by TSOs to solve power system operation (e.g., unit commitment) and planning problems. For these reasons, the dynamic performance obtained using the MILP-based scheduling is utilized as a reference in this study. Simulation results are presented in Section A.2 of the ANNEX.

3.3 Co-Simulation Framework

Co-simulation allows studying the dynamic behavior of modern power systems by coupling different sub-domain models, e.g. power systems and electricity markets [21]. Figure 7 shows the structure of the co-simulation framework presented in [22]. Such a framework merges together the model of the sub-hourly stochastic Security-Constrained Unit Commitment (sSCUC), the model of MILP- and AGC-based VPPs, as well as the dynamic model of power systems described in the previous section. A rolling horizon approach is used to feed back the current values of the demand, e.g. $d_{j,t}$, to the sub-hourly sSCUC problem. The reader interested in the complete formulation of the sub-hourly sSCUC is referred to [23]. The solutions of the sSCUC ($p_{i,t}$, $\forall i$) and the regulating signals ($\mathcal{R}_i \Delta p / \mathcal{R}_{\text{tot}}$) generated by the AGC, are utilized to change the power set point of the TGs of the power plants.

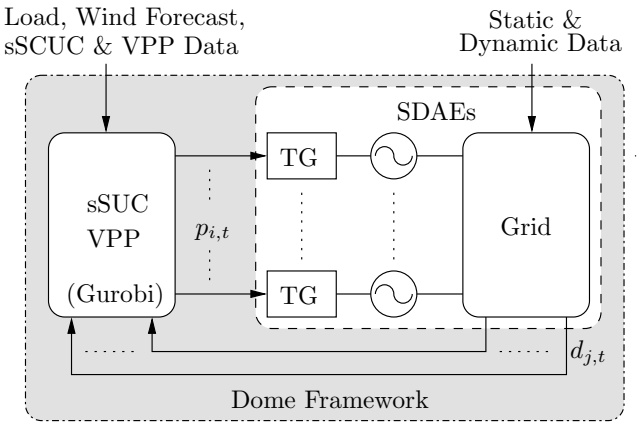

Figure 7 – Co-simulation framework that includes the sub-hourly sSCUC and the models of the grid and the DERs that compose the VPP

3.4 Simulation Results

The proposed AGC-based VPP is tested by considering Use Case FC_B.2 defined in deliverable D2.1. In particular, the New England system is modified to include an AGC implemented as a perfect tracking integral controller. Moreover, the modified system considered includes dynamic

models of wind power plants and VPPs. In particular, 25% wind penetration level is considered, where the wind generation is given by wind power plants connected to buses 20-23. Wind power plants are represented by aggregated models, which implement a 5-th order Doubly-Fed Induction Generator (DFIG) model with voltage, pitch angle and Maximum Power point Tracking (MPPT) controllers [24]. The modeling of the stochastic nature of wind is as described in the ANNEX of deliverable D2.1. To simulate the VPP, 10 small generators are connected to buses 10-19. In the following, we assume that the VPP is only composed of non-renewable generation, i.e. small gas power plants. This is the case e.g. of the Irish system. Furthermore, in order to create a realistic case study, the real-world data of the VPP made available by EirGrid for the Irish power system [14] are utilized. The VPP penetration level considered is 20%, which is relevant for future grids with high penetration of DERs.

Simulation results are presented in Section A.2 of the ANNEX.

4. Frequency Regulation Metering During Transients

4.1 Introduction

A current challenge for the secure operation of the grid is the ability of TSOs to determine through simple measurements whether a device connected to the grid provides frequency control at a given time [19, 25, 26]. The need for metrics to define the frequency response and control in a transmission system has been recognized since a decade ago. The report [27], for example, defines three obvious metrics, namely frequency nadir, nadir-based frequency response, and primary frequency response. These are, however, "global" metrics and are adequate only for off-line adequacy and reliability studies. Existing techniques to evaluate the primary frequency and inertial responses are qualitative and based on statistical analysis of time series [28, 29] or on Kalman filtering [30].

To date, there is no direct way to verify whether a given device is actually providing frequency control at a given time or not. This prevents system operators from relying on and properly rewarding the devices that provide such frequency support. Smart metering is already a reality but it is mostly utilized on the device side to implement the frequency control itself, e.g. [31], rather than on the system operator side. Some TSOs have resolved the problem by measuring the active power output to estimate their mileage. Other TSOs "trust" the operators of power plants, which might expose the system to security issues if the control is not provided or available when needed. A third approach consists in allocating conventional frequency reserve, which guarantees a secure operation but leads to higher energy costs.

This chapter addresses this problem by proposing an index to differentiate between devices that have and do not have an impact on the frequency at their point of connection based on their RoCoP [32, 33]. The proposed technique has been dropped to WP4 as containerized software code and has been integrated into the edgeFLEX platform, in the context of the relation of WP2 with tasks T4.1-T4.3 of WP4.

4.2 Frequency Divider Formula

The relation between current injections, bus voltages and SM Electromotive Forces (EMFs) behind the internal reactances in a power system can be formulated as follows:

$$\begin{bmatrix} \bar{\boldsymbol{i}}_{\mathrm{G}}(t) \\ \bar{\boldsymbol{i}}_{\mathrm{B}}(t) \end{bmatrix} = \begin{bmatrix} \bar{\mathbf{Y}}_{\mathrm{GG}} & \bar{\mathbf{Y}}_{\mathrm{GB}} \\ \bar{\mathbf{Y}}_{\mathrm{BG}} & \bar{\mathbf{Y}}_{\mathrm{BB}} \end{bmatrix} \begin{bmatrix} \bar{\boldsymbol{e}}_{\mathrm{G}}(t) \\ \bar{\boldsymbol{v}}_{\mathrm{B}}(t) \end{bmatrix} , \tag{4.1}$$

where the subscripts G and B stand for synchronous generation buses, and for load and transition buses, respectively; $\bar{\boldsymbol{v}}_{\mathrm{B}}(t)$ and $\bar{\boldsymbol{i}}_{\mathrm{B}}(t)$ are bus voltages and current injections, respectively, at network buses; $\bar{\boldsymbol{i}}_{\mathrm{G}}(t)$ are generator current injections; $\bar{\boldsymbol{e}}_{\mathrm{G}}(t)$ are generator EMFs behind the internal generator impedance; $\bar{\mathbf{Y}}_{\mathrm{GG}} \in \mathbb{C}^{m\times m}$; $\bar{\mathbf{Y}}_{\mathrm{BB}} \in \mathbb{C}^{n\times n}$; $\bar{\mathbf{Y}}_{\mathrm{GB}} \in \mathbb{C}^{m\times n}$; and $\bar{\mathbf{Y}}_{\mathrm{BG}} \in \mathbb{C}^{n\times m}$. The sub-matrix $\bar{\mathbf{Y}}_{\mathrm{BB}}$ is defined as $\bar{\mathbf{Y}}_{\mathrm{BB}} = \bar{\mathbf{Y}}_{\mathrm{bus}} + \bar{\mathbf{Y}}_{\mathrm{G}}$, where $\bar{\mathbf{Y}}_{\mathrm{bus}}$ is the well-known network admittance matrix, and $\bar{\mathbf{Y}}_{\mathrm{G}}$ is a diagonal matrix whose h-th diagonal element is zero if no machine is connected to bus h; and the inverse of $jx_{\mathrm{G},h}$ if a machine is connected to bus h. $x_{\mathrm{G},h}$ is the machine internal transient reactance and includes the reactance of the step-up transformer of the machine if this is not part of the network topology.

Having as starting point the expression (4.1), the Frequency Divider Formula (FDF) as derived in [34] proposes that SM rotor speeds and frequency variations of network buses in a power system are linked as follows:

$$\mathbf{B}_{\mathrm{BG}} \Delta\boldsymbol{\omega}_{\mathrm{G}}(t) = -\mathbf{B}_{\mathrm{BB}} \Delta\boldsymbol{\omega}_{\mathrm{B}}(t) \,, \tag{4.2}$$

where $\Delta\boldsymbol{\omega}_{\mathrm{G}}(t) \in \mathbb{R}^m$ is the vector of machine rotor speed variations; $\Delta\boldsymbol{\omega}_{\mathrm{B}}(t) \in \mathbb{R}^n$ are the frequency variations at the system buses; and $\mathbf{B}_{\mathrm{BG}} = \Im\{\bar{\mathbf{Y}}_{\mathrm{BG}}\}$ and $\mathbf{B}_{\mathrm{BB}} = \Im\{\bar{\mathbf{Y}}_{\mathrm{BB}}\}$. $\mathbf{B}_{\mathrm{BB}}$ can be obtained from $\mathbf{B}_{\mathrm{bus}} = \Im\{\bar{\mathbf{Y}}_{\mathrm{bus}}\}$ as $\mathbf{B}_{\mathrm{BB}} = \mathbf{B}_{\mathrm{bus}} + \mathbf{B}_{\mathrm{G}}$, where $\mathbf{B}_{\mathrm{G}} = \Im\{\bar{\mathbf{Y}}_{\mathrm{G}}\}$. In (4.2), frequency variations are in per unit with respect to the system reference frequency.

4.3 Regulating Power and RoCoP

The complex power injection at the network buses of a system, say $\bar{\boldsymbol{s}}_{\mathrm{B}}$, can be expressed in terms of the well-known power flow equations, as follows:

$$\bar{\boldsymbol{s}}_{\mathrm{B}}(t) = \boldsymbol{p}_{\mathrm{B}}(t) + j\boldsymbol{q}_{\mathrm{B}}(t) = \bar{\boldsymbol{v}}_{\mathrm{B}}(t) \circ \left[\bar{\mathbf{Y}}_{\mathrm{bus}}\, \bar{\boldsymbol{v}}_{\mathrm{B}}(t)\right]^{*} , \tag{4.3}$$

where $\circ$ is the Hadamard product, i.e., the element-by-element product of two vectors. For the sake of derivation, it is convenient to rewrite (4.3) in an element-wise notation and extract the active power:

$$p_{\mathrm{B},h}(t) = v_{\mathrm{B},h}(t) \sum_{k\in\mathbb{B}} v_{\mathrm{B},k}(t)\, G^{hk}_{\mathrm{bus}}\, \cos\theta_{\mathrm{B},hk}(t) + v_{\mathrm{B},h}(t) \sum_{k\in\mathbb{B}} v_{\mathrm{B},k}(t)\, B^{hk}_{\mathrm{bus}}\, \sin\theta_{\mathrm{B},hk}(t) , \tag{4.4}$$

where $\mathbb{B}$ is the set of network buses; G^{hk}_{bus} and B^{hk}_{bus} are the real and imaginary parts of the element (h,k) of the network admittance matrix, i.e. $\bar{Y}^{hk}_{\mathrm{bus}} = G^{hk}_{\mathrm{bus}} + jB^{hk}_{\mathrm{bus}}$; $v_{\mathrm{B},h}$ and $v_{\mathrm{B},k}$ denote the voltage magnitudes at buses h and k, respectively; and $\theta_{\mathrm{B},hk}(t) = \theta_{\mathrm{B},h}(t) - \theta_{\mathrm{B},k}(t)$, where $\theta_{\mathrm{B},h}(t)$ and $\theta_{\mathrm{B},k}(t)$ are the voltage phase angles at buses h and k, respectively. Let us differentiate (4.4) and write the active power injections as the sum of two components:

$$dp_{\mathrm{B},h} = \sum_{k\in\mathbb{B}} \frac{\partial p_{\mathrm{B},h}}{\partial \theta_{\mathrm{B},k}}\, d\theta_{\mathrm{B},k} + \sum_{k\in\mathbb{B}} \frac{\partial p_{\mathrm{B},h}}{\partial v_{\mathrm{B},k}}\, dv_{\mathrm{B},k} = dp'_{\mathrm{B},h} + dp''_{\mathrm{B},h} , \tag{4.5}$$

In (4.5), $dp_{\mathrm{B},h}$ is the total variation of power at bus h, while $dp'_{\mathrm{B},h}$ is what, in the deliverable, we call "regulating power". In general, $dp_{\mathrm{B},h} \neq dp'_{\mathrm{B},h}$, so $p'_{\mathrm{B},h}(t)$ cannot be measured directly, except for some special cases that are discussed in Section 4.4. This is why an approach to determine $p'_{\mathrm{B},h}(t)$ indirectly based on frequency measurements is proposed in this deliverable. The second term in (4.5), namely $p''_{\mathrm{B},h}(t)$, by definition, does not depend on phase angle variations and thus plays no role in altering the frequency of the buses and thus is not further considered in the remainder of this deliverable. As a matter of fact, it appears that $p''_{\mathrm{B},h}(t)$ is the quota of the active power that behaves as a passive admittance [32].

While one can use the expression of $dp'_{\mathrm{B},h}$ as is, i.e., as a non-linear function of voltage magnitudes and phase angles, we have observed that the dependency on such quantities can be simplified without compromising its accuracy, as follows.

- The first term in (4.5), namely $dp'_{\mathrm{B},h}$, is the one that varies the most when the active power at bus h is regulated, whereas the contribution to the active power regulation of the second term, namely $dp''_{\mathrm{B},h}$, is negligible, if any at all.
- The differentiation of $dp'_{\mathrm{B},h}$ with respect to time can be conveniently approximated with:

$$\dot{p}'_{\mathrm{B},h}(t) \approx \Omega_b \sum_{k\in\mathbb{B}} B^{hk}_{\mathrm{bus}} \left[\omega_{\mathrm{B},h}(t) - \omega_{\mathrm{B},k}(t)\right] , \tag{4.6}$$

  where $\omega_{\mathrm{B},k}(t) = \Omega_b^{-1}\dot{\theta}_{\mathrm{B},k}(t)$ is the frequency in pu(rad/s) at bus k; Ω_b is the reference synchronous speed in rad/s; and where it is assumed:

$$\frac{\partial p'_{\mathrm{B},h}}{\partial \theta_{\mathrm{B},k}} \approx B^{hk}_{\mathrm{bus}} . \tag{4.7}$$

The two assumptions above have been thoroughly tested considering:

- Several networks of different size (from three to thousands of buses) and topology (both transmission and distribution systems);
- A large variety of devices ranging from conventional SMs and loads to non-synchronous generators based on wind and solar as well as converter-based ESSs with and without frequency control.

- A variety of faults and large disturbances, including three-phase faults, and device outages.

In all cases, the approximation assumed in (4.7) has proven to be extremely good, which leads to conclude that the effect of voltage magnitudes is effectively negligible, if any at all. Therefore, the accuracy and effectiveness of the approach proposed in the deliverable have been confidently proven.

Using a vector-based notation, the injection of regulating power $\boldsymbol{p}'_{\mathrm{B}}(t)$ into the network buses can be approximated as [32]:

$$\boldsymbol{p}'_{\mathrm{B}}(t) = -\mathbf{B}_{\mathrm{bus}}\boldsymbol{\theta}_{\mathrm{B}}(t)\,, \tag{4.8}$$

which appears to have the same formal expression as the well-known DC power flow problem [35, 36]. It is important to note, however, that in the DC power flow the term on the left-hand side of the equation is the *total* power. Instead in (4.8), the term on the left-hand side is only a quota of the active power. Differentiating (4.8) with respect to time gives the most important equation of this chapter, which in turn is the vector-based notation of (4.6):

$$\dot{\boldsymbol{p}}'_{\mathrm{B}}(t) = -\Omega_b\mathbf{B}_{\mathrm{bus}}\Delta\boldsymbol{\omega}_{\mathrm{B}}(t) = -\hat{\mathbf{B}}_{\mathrm{bus}}\Delta\boldsymbol{\omega}_{\mathrm{B}}(t)\,. \tag{4.9}$$

The vector $\dot{\boldsymbol{p}}'_{\mathrm{B}}(t)$ represents the RoCoP injections into the system nodes. This quantity is not trivially the numerical derivative of the active power injection/consumption at network buses as $\boldsymbol{p}_{\mathrm{B}}(t) = \boldsymbol{p}'_{\mathrm{B}}(t) + \boldsymbol{p}''_{\mathrm{B}}(t)$ and, in general, $\boldsymbol{p}''_{\mathrm{B}}(t) \neq 0\ \forall t$. Expression (4.9) indicates that a time-varying active power injection into the network bus modifies the frequency at that bus. Noteworthy, such active power variation can be originated by devices other than just SMs. This concept is further elaborated in the remainder of this chapter.

Expression (4.9) can be perceived as a generalization of (4.2). the FDF (4.2) can be derived from (4.9), IF we put together (4.2) and (4.9), which gives [32]:

$$\dot{\boldsymbol{p}}'_{\mathrm{B}}(t) = -\hat{\mathbf{B}}_{\mathrm{BG}}\left[\Delta\boldsymbol{\omega}_{\mathrm{G}}(t) - \Delta\boldsymbol{\omega}_{\mathrm{BG}}(t)\right]\,, \tag{4.10}$$

where $\hat{\mathbf{B}}_{\mathrm{BG}} = \Omega_b\mathbf{B}_{\mathrm{BG}}$. Equivalently:

$$\mathbf{B}_{\mathrm{BG}}\left[\Delta\boldsymbol{\omega}_{\mathrm{G}}(t) - \Delta\boldsymbol{\omega}_{\mathrm{BG}}(t)\right] = -\mathbf{B}_{\mathrm{bus}}\Delta\boldsymbol{\omega}_{\mathrm{B}}(t)\,, \tag{4.11}$$

where $\Delta\boldsymbol{\omega}_{\mathrm{BG}}(t) \subset \Delta\boldsymbol{\omega}_{\mathrm{B}}(t)$ is the subset of frequency deviations at the terminal buses of the SMs. The two formulations of the FDF (4.2) and (4.9) are complementary and will be used in this chapter to show the properties of devices that modify, locally, the frequency by providing either inertial or fast frequency response, and later in Chapter 5 to derive an expression to estimate inertia.

4.4 Taxonomy of Devices Based on their RoCoP

The observation that motivates the technique presented in this chapter originates from the structure of the revisited FDF given in (4.11). First, let us consider the simple example of Figure 8, where a SM is connected in antenna to the grid through a transmission line.[1] In this example the step-up transformer is included in the machine model, hence $x_{\mathrm{G}} = x'_{\mathrm{d}} + x_{\mathrm{T}}$.

In Figure 8, bus 1 is the terminal bus of the generator that is accessible and "measurable" by the TSO, whereas bus 2 is the high-voltage neighboring bus at the receiving end of the transmission line that connects the generator to the rest of the grid. Note that the step-up transformer could be also used as the "antenna" connection, provided that both windings are measurable by the TSO. The developments discussed in this section are valid independently on how the step-up transformer is modeled, either internally to the machine or externally as part of the grid.

Applying (4.11) to bus 1 of the scheme of Figure 8 leads to:

$$b_{\mathrm{G}}[\Delta\omega_{\mathrm{G}}(t) - \Delta\omega_{\mathrm{B},1}(t)] = (b_{12} + b_{10})\Delta\omega_{\mathrm{B},1}(t) - b_{12}\Delta\omega_{\mathrm{B},2}(t)\,, \tag{4.12}$$

[1] The antenna configuration is used for simplicity but any topology can be used. The general case is considered in (4.15).

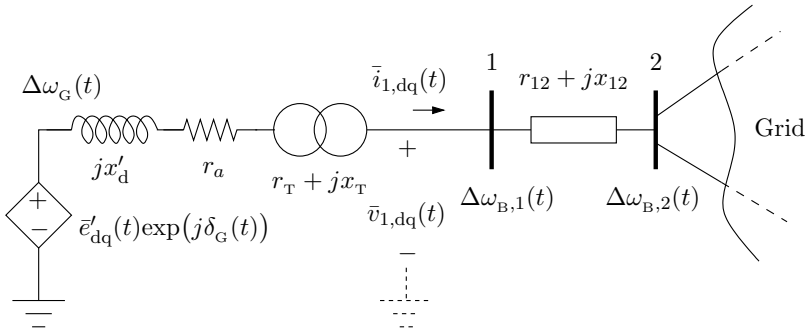

Figure 8 – Synchronous machine connected in antenna to the grid

where $b_{\mathrm{G}} = 1/x_{\mathrm{G}}$ is the internal susceptance of the SM and step-up transformer; b_{10} is the shunt susceptance at bus 1 and $b_{12} = 1/x_{12}$ is the susceptance of the branch that connects buses 1 and 2. In (4.12), the signs are a consequence of (4.11) and of assuming b_{G} and b_{12} to be positive if inductive.

Equation (4.12) is written with the knowledge that the device connected to bus 1 is a SM, which imposes the frequency at the EMF behind the susceptance b_{G}. Moreover, for simplicity, we only consider the topology illustrated in Figure 8. The properties of devices that do and do not modify locally the frequency discussed below, in fact, do not depend on the number of connections of such devices to the grid. The case of multiple connections can be readily taken into account and, as a matter of fact, a general topology is considered for the RoCoP definition given in (4.15).

Let us now assume that we do not know anything of the device connected to bus 1 (*black box*) but some measurements at its terminal bus. This case is shown in Figure 9.

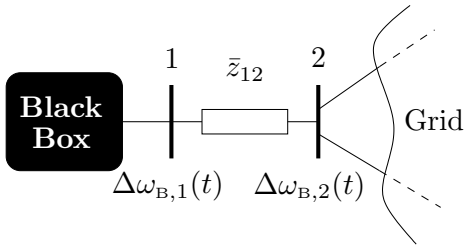

Figure 9 – Black-box device connected in antenna to the grid

Regardless of the actual behavior of the black box, we can rewrite (4.12) by assuming that the black box has an internal frequency, $\Delta\omega_{\mathrm{bb}}(t)$, and an equivalent, possibly time-variant susceptance, $b_{\mathrm{bb}}(t)$, both unknown:

$$b_{\mathrm{bb}}(t)[\Delta\omega_{\mathrm{bb}}(t) - \Delta\omega_{\mathrm{B},1}(t)] = b_{12}[\Delta\omega_{\mathrm{B},1}(t) - \Delta\omega_{\mathrm{B},2}(t)] \,, \tag{4.13}$$

where, consistently with the assumptions that lead to the FDF and without loss of generality, $b_{12} \gg b_{10}$ is assumed. The term $b_{\mathrm{bb}}(t)[\Delta\omega_{\mathrm{bb}}(t) - \Delta\omega_{\mathrm{B},1}(t)]$ in (4.13) is not known. According to (4.10), (4.13) can be also written as:

$$\dot{p}'_{\mathrm{B},1}(t) = \hat{b}_{12}\left[\Delta\omega_{\mathrm{B},1}(t) - \Delta\omega_{\mathrm{B},2}(t)\right] , \tag{4.14}$$

where $\hat{b}_{12} = \Omega_b b_{12}$ and $\dot{p}'_{\mathrm{B},1}(t)$ is the RoCoP at the bus of connection of the black-box device with the grid. Expression (4.14) can be conveniently generalized by assuming that there is more than one branch connected to the monitored bus. Hence, assuming to monitor the h-th bus, the proposed general formula to discriminate between devices that modify the frequency at their POC and devices that do not is:

$$\dot{p}'_{\mathrm{B},h}(t) = \sum_{k\in\mathbb{B}} \hat{b}_{hk}\left[\Delta\omega_{\mathrm{B},h}(t) - \Delta\omega_{\mathrm{B},k}(t)\right] , \tag{4.15}$$

where $\mathbb{B}$ is the set of buses connected to bus h and b_{hk} is the susceptance of the branch connecting

bus h to bus k. Equation (4.15) only requires the knowledge of the system admittance matrix and the measurement/estimation of the frequencies at the neighboring buses of the device to be monitored. This information is easily available to the TSOs. No confidential information about the device itself has to be provided. In (4.15), the term $\sum_{k\in\mathbb{B}} \hat{b}_{hk}\Delta\omega_{\mathrm{B},h}(t)$ represents the combined effect on the frequency of both the device connected to bus h and the rest of the network; whereas the term $\sum_{k\in\mathbb{B}} \hat{b}_{hk}\Delta\omega_{\mathrm{B},k}(t)$ represents the effect of the whole network on the frequency at bus h. Subtracting the latter to the former, what remains is the effect of the black-box device on the frequency variation at bus h.

Next, we discuss some special cases of (4.15), and provide a taxonomy of devices based on their ability to modify the frequency at their POC.

4.4.1 Devices that Do Not Modify the Frequency

According to our definition, the devices that are unable to modify the frequency at their POC satisfy the condition $\dot{p}'_{\mathrm{B},h}(t) = 0, \forall t$, because there cannot be any variation of frequency within a passive circuit (boundary conditions on the frequency are imposed externally from the device). For such devices, thus, the following relationship holds:

$$\Delta\omega_{\mathrm{bb},h}(t) \equiv \Delta\omega_{\mathrm{B},h}(t)\,,\ \forall t\,. \tag{4.16}$$

Constant admittance loads fall in this category. However, for most devices, the condition $\dot{p}'_{\mathrm{B},h}(t) = 0$ is too strict. We thus relax it and assume that a device is unable to modify the frequency at its POC if it satisfies the condition:

$$|\dot{p}'_{\mathrm{B},h}(t)| \approx \left|\frac{\Delta p_{\mathrm{B},h}(t)}{\Delta t}\right| < \epsilon\,, \tag{4.17}$$

where $\epsilon > 0$ is a given empirical threshold that, once agreed upon by all parties, can be used by the TSO to define network codes and ancillary services.

Condition (4.17) can be satisfied in two relevant cases:

1) Slow Power Variations: The device does vary its power consumption/production, but the RoCoP is small in the considered time frame of PFC. According to the notation of (4.17), this situation is characterized by a non-negligible $\Delta p_{\mathrm{B},h}(t)$ and a *large* Δt. For instance, the SFC or the daily ramp-up of loads do not significantly vary the frequency at the buses.

2) Small Power Variations: No load consumption or generation is ever perfectly constant. Stochastic white noise, at least, creates local tiny fluctuations. If the noise is small enough, however, such variations are unable to impact on the frequency. According to the notation of (4.17), this situation is characterized by *small* $\Delta p_{\mathrm{B},h}(t)$ per unit of time. In [32], it is shown that constant admittance loads have $\dot{p}'_{\mathrm{B},h}(t) = 0\ \forall t$. For non-linear loads, this condition does not hold in general. However, independently from the load voltage dependency, we can assume that a load can be modeled as two components, one slowly time-varying ramp, $p_{\mathrm{ramp}}(t)$, and a stochastic component, $p_{\mathrm{stoch}}(t)$ (see, for example, the model described in [37]), i.e. $p_{\mathrm{L}}(t) = p_{\mathrm{ramp}}(t) + p_{\mathrm{stoch}}(t)$, then $\dot{p}_{\mathrm{L}}(t)$ will be negligible, even though the load consumption is not perfectly constant.

4.4.2 Devices that Modify the Frequency

According to our definition, a device is able to vary the local frequency whenever the condition $\dot{p}'_{\mathrm{B},h}(t) \neq 0$ holds. Following the discussion above, the only variations of power of interest are those that are sufficiently big to be able to vary the local frequency above a certain threshold and sufficiently fast to be comparable to the time scale of the inertial response and PFC of SMs. Using the same notation as in (4.17), a device is able to modify the frequency at its bus of connection if the following condition is satisfied:

$$|\dot{p}'_{\mathrm{B},h}(t)| \approx \left|\frac{\Delta p_{\mathrm{B},h}(t)}{\Delta t}\right| \geq \epsilon\,. \tag{4.18}$$

In the following, we consider various technologies.

1) Synchronous Machines: The dynamics of the rotor speed of a machine connected to bus h can be approximated by:

$$M_{\mathrm{G}}\dot{\omega}_{\mathrm{G}}(t) = p_m(t) - p_{\mathrm{B},h}(t) \ , \tag{4.19}$$

where M_{G} is the mechanical starting time and $p_m(t)$ is the mechanical power provided by the turbine. The mechanical power can be decomposed into three terms:

$$p_m(t) = p_{\mathrm{UC}}(t) + p_{\mathrm{PFC}}(t) + p_{\mathrm{SFC}}(t) \ , \tag{4.20}$$

where $p_{\mathrm{UC}}(t)$ is the power set point as defined by the solution of the unit commitment problem; $p_{\mathrm{PFC}}(t)$ is the active power regulated by the PFC; and $p_{\mathrm{SFC}}(t)$ is the active power regulated by the SFC. For a typical SM, the PFC is achieved through a TG, and the SFC is achieved through AGC.

Hence, the active power injected by an SM into its terminal bus can be written as:

$$p_{\mathrm{B},h}(t) = p_{\mathrm{UC}}(t) + p_{\mathrm{PFC}}(t) + p_{\mathrm{SFC}}(t) - M_{\mathrm{G}}\dot{\omega}_{\mathrm{G}}(t) \ , \tag{4.21}$$

where $p_{\mathrm{UC}}(t)$ is piece-wise constant and $p_{\mathrm{SFC}}(t)$ varies slowly. Hence, of the four components above, the ones that actually contribute to modify the frequency at the machine bus are $p_{\mathrm{PFC}}(t)$ and the machine inertial response. Therefore:

$$\dot{p}'_{\mathrm{B},h}(t) \approx \dot{p}_{\mathrm{PFC}}(t) - M_{\mathrm{G}}\ddot{\omega}_{\mathrm{G}}(t) \ . \tag{4.22}$$

In the very first instants after a contingency the dominant effect is due to the inertial response but, in general, the two terms are intertwined. Note, however, that if a machine does not provide PFC, then the lack of regulation can be inferred by observing the transient behavior of $\dot{p}'_{\mathrm{B},h}(t)$, as illustrated in the examples of Section A.3.2.

2) Non-Synchronous Devices: This category includes, but not limited to, grid-forming power electronics converters of non-synchronous generation and ESSs, and TCLs. Such devices consist of a frequency control loop, with a given reference frequency, ω^{ref}, as illustrated in Figure 10.

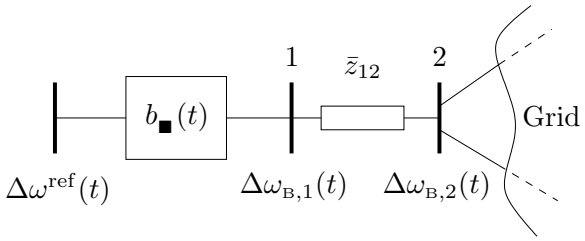

Figure 10 – Example of a device that controls the frequency at bus 1

The actual implementation of the controller, which is accounted for with a time-dependent susceptance, $b_{\mathrm{bb}}(t)$, is unknown. However, regardless of its transfer function, the controller tracks a reference frequency, so, in turn, $\Delta\omega_{\mathrm{bb},h}(t) = \Delta\omega^{\mathrm{ref}}(t)$. In practice, ω^{ref} is constant and, hence, $\Delta\omega^{\mathrm{ref}} = 0$. While not known in detail, we can assume that $b_{\mathrm{bb}}(t) \neq 0$ and $\dot{p}'_{\mathrm{B},h}(t) \neq 0$ for any transient condition for which $\Delta\omega_{\mathrm{B},h}(t) \neq \Delta\omega^{\mathrm{ref}}$.

Next, we present two relevant cases: (i) WTs with frequency control, and (ii) ESSs.

For a WT, one has:

$$p_{\mathrm{B},h}(t) = p_{\mathrm{stoch}}(t) + p_{\mathrm{PFC}}(t) \ , \tag{4.23}$$

where the stochastic term $p_{\mathrm{stoch}}(t)$ depends on the uncertainty and volatility of the wind speed and the second term $p_{\mathrm{PFC}}(t)$ is given by the primary frequency controller of the WT, if any. Large and fast stochastic variations, such as wind gusts, are indistinguishable, in principle, from power variations aimed at regulating the frequency. The only difference is statistical. Wind gusts, in fact, will show for about 50% of the times a variation that further increases the actual frequency deviation. Instead,

a power variation imposed by a frequency controller always aims at tracking the synchronous frequency. Wind gusts, however, are relatively uncommon and, very often, WPPs are not operated at their maximum capacity.[2] Moreover, typical values of the autocorrelation coefficients of wind speeds (see, for example, [39]) lead to conclude that wind turbulences have a small local effect on active power fluctuations, whereas the average value of the wind varies quite slowly with time. Thus, except for rare strong wind gusts, the RoCoP of a wind turbine can be assumed to be:

$$\dot{p}'_{\mathrm{B},h}(t) \approx \dot{p}_{\mathrm{stoch}}(t) + \dot{p}_{\mathrm{PFC}}(t) \approx \dot{p}_{\mathrm{PFC}}(t) \ , \tag{4.24}$$

at least for all variations such that $|\dot{p}'_{\mathrm{B},h}(t)| > \epsilon_{\mathrm{WT}}$, where the threshold ϵ_{WT} can be chosen based on statistical properties (shape factor and autocorrelation) of the wind at the location of the WPP. This important point is further discussed in Section 4.6.

The case of ESSs is probably the easiest one to analyze. These devices are based on deterministic controllers and, when used to provide primary frequency support, they generate/absorb power only if the frequency is outside a band around the synchronous reference speed:

$$p_{\mathrm{B},h}(t) = p_{\mathrm{PFC}}(t) \quad \Rightarrow \quad \dot{p}'_{\mathrm{B},h}(t) = \dot{p}_{\mathrm{PFC}}(t) \ . \tag{4.25}$$

4.5 Dynamic State Estimation

This section discusses the consequences of (4.9) and (4.15) for the dynamic state estimation of bus frequencies (Subsection 4.5.1) and machine rotor speeds (Subsection 4.5.2).

4.5.1 Bus Frequencies

The estimation of bus frequencies is conventionally based on the measurements of bus voltage phasors and the proper design of Phase-Locked Loops (PLLs), which are part of Phasor Measurement Units (PMUs) or equivalent devices. To achieve a satisfactory level of accuracy with this type of estimation is possible but challenging [40]. Expression (4.9) suggests that active power measurements can be utilized to estimate frequency variations at network buses. From (4.9), one has:

$$\Delta\boldsymbol{\omega}_{\mathrm{B}}(t) = -\hat{\mathbf{B}}_{\mathrm{bus}}^{-1}\, \dot{\boldsymbol{p}}'_{\mathrm{B}}(t) \ , \tag{4.26}$$

where $\dot{\boldsymbol{p}}'_{\mathrm{B}}(t)$ can also be approximated with $\Delta\boldsymbol{p}_{\mathrm{B}}/\Delta t$ in a given finite time Δt. *Vice versa*, based on (4.15), if frequency estimations at network buses are known, the regulating power provided by a device can be estimated as:

$$\Delta p'_{\mathrm{B},h}(t) = \int_t \sum_{k\in\mathbb{B}} \hat{b}_{hk} \left[\Delta\omega_{\mathrm{B},h}(\tau) - \Delta\omega_{\mathrm{B},k}(\tau)\right] d\tau \ . \tag{4.27}$$

4.5.2 Machine Rotor Speed

In [41], it was described how to estimate the rotor speeds of SMs based on the FDF. The noteworthy result of [41] is that such an estimation can be achieved with a reduced set of bus frequency estimations and a linear optimization problem. Considering the example of Figure 8, the rotor speed of the machine can be obtained as:

$$\Delta\omega_{\mathrm{G}}(t) = \frac{b_{12} + b_{\mathrm{G}}}{b_{\mathrm{G}}}\, \Delta\omega_{\mathrm{B},1}(t) - \frac{b_{12}}{b_{\mathrm{G}}}\, \Delta\omega_{\mathrm{B},2}(t) \ . \tag{4.28}$$

Equation (4.10) leads to an alternative expression to estimate the rotor speed of the machine based only on measurements at the terminal bus of the machine itself (thus also eliminating the issue of

[2] See, for example, the so-called "wind dispatch down" periods defined by EirGrid and SONI, that effectively make constant the power production of a WPP [38].

measurement delays discussed in [41]):

$$\Delta\omega_{\mathrm{G}}(t) = \Delta\omega_{\mathrm{B},1}(t) - \hat{x}_{\mathrm{G}}\dot{p}'_{\mathrm{B},1}(t) \ , \tag{4.29}$$

where $\hat{x}_{\mathrm{G}} = 1/\hat{b}_{\mathrm{G}}$. The former expression can be also used for any radial connection, such as a long transmission line, to estimate the frequency at one end by measuring the frequency and the active power injection into the other end.

4.6 Statistical Interpretation of the RoCoP

We have proposed a taxonomy of devices based on their ability to vary the frequency at their POC with the grid. In particular, a device is assumed to be able to modify the frequency if it satisfies the condition (4.18). In (4.18), the definition of the threshold ϵ has to take into account the dynamic behavior of the device. We have discussed that this can be done considering the rate of change and the magnitude of the power variations. Based on that, we further discuss two relevant cases: (i) stochastic fluctuations of the power source, such as the wind speed; and (ii) measurement noise.

The statistical properties of the wind can be properly determined based on time series of wind speed measurements [42, 43]. Similarly, the volatility of other RESs can be studied through stochastic differential equations, e.g., the effect of clouds on the solar irradiance [44] and of the swell phenomenon on tidal currents [45]. The most relevant information from these models is the standard deviation of the fluctuations and the autocorrelation coefficient. The latter indicates, on a statistical basis, how much the wind speed is going to change from one value to another in a given time. Roughly speaking, the autocorrelation coefficient of a stochastic process is the equivalent of the time constant of a first-order differential equation [39].

From the standard deviation of the stochastic process, one can adjust the value of the threshold ϵ in (4.18). On the other hand, the references above indicate that the autocorrelation of the stochastic processes of RESs leads to variations whose time scales are either slower (e.g., clouds and swell phenomenon) or faster (e.g., wind short-term fluctuations) than the FFR and are naturally filtered by the turbines and/or the regulators of the DERs. Similarly, the noise of the measurements of the bus frequencies tends to be much faster than the inertial response and FFR. Such a noise can thus be filtered without affecting the reliability of the RoCoP.

4.7 Remarks

This section discusses some relevant remarks.

- *Impact of Latency:* Latency is a well-known issue when dealing with PMU measurements and communication systems [46]. In this case, however, delays do not prevent the proposed RoCoP index to be accurate. The calculation of (4.15), in fact, does not need to be in real-time as it is not utilized for control but, rather, for monitoring and *a posteriori* reward of ancillary services. Since PMU measurements come with a time stamp which is synchronized with the GPS signal, the evaluation of $\dot{p}'_{\mathrm{B},h}(t)$ is virtually unaffected by communication delays, packet loss, etc.
- *Impact of Branch Impedances:* The proposed RoCoP index works better the higher are the differences between the frequency variations $\Delta\omega_{\mathrm{B},h}(t)$ and $\Delta\omega_{\mathrm{B},k}(t)$ of (4.15). Note that the inverse of the impedance of the branches (lines or transformers) that connect the monitored bus to the grid 'amplifies' such differences. If a branch impedance is too small and, hence, the accuracy with which frequency variations have to be measured is too high, one can utilize measurements at further buses as described in the discussion of equation (4.27).
- *Impact of the Time Integration Step:* The performance of the proposed index does not depend on the time integration step of the presented simulations, as long as such integration step is sufficiently small to capture the dynamics of interest. Taking into account the fact that the range of time integration steps considered in the example above lie in the typical sampling rates of measurement devices currently deployed, then this remark can be

extended to real-life scenarios. In other words, the performance of the proposed RoCoP index is independent of the sampling rate of measurement units.

- *Impact of Frequency Measurements Accuracy:* The need for precise frequency measurements may appear as a limitation of the proposed technique. However, in recent years, the accuracy and precision of frequency measurements has been improved significantly. In the simulation tests presented in Section A.3 of the ANNEX, frequency estimation is obtained based on PLLs, as these are ubiquitous in power converters [47, 48]. While it is known that, in some cases, PLLs can create dynamic issues, e.g. [49, 50], other promising methods, in particular those based on some variant of interpolated discrete Fourier transform have been recently shown to be very precise. The interested reader can find a discussion on this approach in [40, 51] and in the references therein. Also the calculation of the Rate of Change of Frequency (RoCoF) has been largely investigated in recent years. Reference [52] provides, along with its own contributions, an introduction to the topic.

4.8 Simulation Results

The features of the proposed RoCoP index are tested considering Use Case FC_D.1 described in deliverable D2.1 and the KPIs defined therein. Simulation tests are presented in Section A.3 of the ANNEX and are obtained using Dome. In these tests, bus frequencies are estimated with SRF-PLLs. The fundamental-frequency model of an SRF-PLL is described in D2.1.

5. Dynamic Inertia Estimation

5.1 Introduction

The replacement of SMs with non-synchronous devices, namely Converter Interfaced Generation (CIG) sources, such as wind and solar, decreases the inertia of the power system [19]. This creates operation and security issues as a minimum inertia is required in the system [53]. Advanced control schemes that make non-synchronous devices provide inertia support have been developed in recent years. Examples are the VSM control [54] and inertial response control [55]. The objective of these controls is to emulate the inertia response in the SMs and thus enforce the non-synchronous devices boosting the power at the instant of the contingency, and therefore, leading to the concept of equivalent inertia. The equivalent inertia of non-synchronous devices, unlike the inertia constant of SMs, may be variable [56], and even be specially designed as time-varying [57]. A general method to fast and accurately estimate both the constant and non-constant (equivalent) inertia, however, is still missing. This chapter aims at developing an on-line inertia estimation approach that can accurately track the (equivalent) inertia of both synchronous and non-synchronous devices.

Efforts have been made to improve the accuracy to estimate the inertia constant for SMs via off-line tests [58, 59, 60]. Similar techniques have been also developed for the off-line identification of the inertia of the turbines of non-synchronous RESs [61, 62]. The inertia of these devices can be uncertain, or even time-varying, due to the ever-changing renewables and converter controls [63]. Off-line tests, therefore, are not enough to track the presented inertia of the non-synchronous devices.

The accurate and precise on-line monitoring for the dynamic behavior of the power system becomes feasible with the development of the smart grid techniques [64], especially, the wide application of PMUs [59, 65]. For example, reference [66] presents a Bayesian framework based on the data collected with PMUs to estimate the inertia of the generators with high accuracy. The high computational burden of the Bayesian method, however, makes its utilization impractical for on-line monitoring. Several PMU-based estimation methods for the equivalent inertia constant of a power system have been developed [67, 68, 69, 70]. Most of them, however, are not adequate tools for the on-line inertia estimation of single devices, especially non-synchronous devices with non-constant inertia control.

Reference [67] proposes an on-line identification algorithm for the equivalent inertia of an entire power system by analyzing its dynamic response to a designed micro-perturbation. Since the micro-perturbation signal affects the frequency response of the system, it may lead to the unexceptional action of the protective relays and thus increase the potential risk of the power system stability. The same limit also exists for the perturbation-needed inertia estimation method proposed in [68]. Reference [69] obtains the system inertia by analyzing the frequency signal via rotational invariance techniques. The analysis requires a precise model that may not be available in real-world applications. Reference [70] avoids the limitations of [67, 68, 69] by proposing an on-line inertia estimator based on the extension and mixture of a dynamic regressor. While this regressor is designed under the assumption that the inertia is constant. Time-varying equivalent inertia, therefore, can prevent above estimation techniques to converge.

5.2 Technical Background

The inertia constant conditions the dynamics of SMs through the well-known swing equation:

$$M_{\mathrm{G}}\,\dot{\omega}_{\mathrm{G}}(t) = p_m(t) - p_{\mathrm{G}}(t) - D_{\mathrm{G}}\left(\omega_{\mathrm{G}}(t) - \omega_o\right), \tag{5.1}$$

where ω_{G} is the rotor speed of the SM; ω_o is the reference angular speed; D_{G} is the damping coefficient; p_{G} is the electrical power of the SM injected into the grid; and p_m is the mechanical power of the SM; and M_{G} is the machine starting time, which is twice the inertia constant, i.e., $M_{\mathrm{G}} = 2H_{\mathrm{G}}$. To avoid carrying around the factor "2", the estimation technique described in this chapter is aimed at determining M_{G}.

During the period of inertial response, the dynamic behavior of the frequency mainly depends on the inertia of the system and is characterized by a relatively high $\dot{\omega}$, often called RoCoF [71]. Following the inertial response, the frequency gradually recovers to the nominal via the PFC and SFC. The inertia estimation approach proposed in this chapter takes advantage of the fact that the inertial response is the fastest among the frequency responses of the SM and the one with the highest RoCoF.

5.3 Dynamic Inertia Estimation Formulation

For the derivation of the inertia estimation formula, it is convenient to split the mechanical power into three components, as in (4.20). Differentiating (5.1) with respect to time and taking into account (4.20), we can deduce:

$$M_{\mathrm{G}}\,\ddot{\omega}_{\mathrm{G}}(t) = \dot{p}_{\mathrm{UC}}(t) + \dot{p}_{\mathrm{PFC}}(t) + \dot{p}_{\mathrm{SFC}}(t) - \dot{p}_{\mathrm{G}}(t) - D_{\mathrm{G}}\,\dot{\omega}_{\mathrm{G}}(t)\ . \tag{5.2}$$

Within the inertial response time scale, we can assume that $\dot{p}_{\mathrm{UC}}(t) \approx 0$, $\dot{p}_{\mathrm{SFC}}(t) \approx 0$. The time scale of the inertial response of the machine is faster than that of its PFC and thus, in the first seconds after an event that causes a power imbalance in the system, we can also assume that $|\dot{p}_{\mathrm{PFC}}(t)| \ll |\dot{p}_{\mathrm{G}}(t)|$. Since p_{G} is the SM grid power injection, it is always measurable by the TSOs. Then, $\dot{p}_{\mathrm{G}}$ can be estimated based on PMUs measurements as discussed in Chapter 4. Finally, based on the estimation technique proposed in [41], we can assume to be able to estimate $\omega_{\mathrm{G}}(t)$ and, thus, be able to calculate $\ddot{\omega}_{\mathrm{G}}(t)$. In the following, we can thus assume that $\dot{p}_{\mathrm{G}}(t)$ and $\ddot{\omega}_{\mathrm{G}}(t)$ are measurable and known. With these assumptions, the following inertia estimation formula is proposed as a byproduct of the RoCoP:

$$M_{\mathrm{G}} \approx M^{*}_{\mathrm{G}} = -\frac{\dot{p}_{\mathrm{G}}(t)}{\ddot{\omega}_{\mathrm{G}}(t)}\ , \tag{5.3}$$

where $*$ indicates an estimated quantity and it is further assumed that $D_{\mathrm{G}} \approx 0$. The former assumption holds in the time scale of the inertial response of SMs. Note that neglecting the damping and PFC is acceptable for SMs but might not be adequate for non-synchronous devices. With this in mind, Section 5.5 proposes a method to eliminate the impact of damping and PFC on the inertia estimation of CIG.

The estimation formula (5.3) can be extended to evaluate the (equivalent) inertia of *any* device that is able to modify the frequency at its POC with the grid, namely those devices whose power injection satisfies the condition:

$$|\dot{p}_{\mathrm{bb}}(t)| > \epsilon_p\ , \tag{5.4}$$

where the subindex bb indicates a *black box* device; and ϵ_p is an empirical threshold to exclude the small frequency fluctuations due to, for example, the stochastic variations of ever-changing RESs such as wind and solar generation. The generalized inertia estimation formula is:

$$M_{\mathrm{bb}}(t) \approx M^{*}_{\mathrm{bb}}(t) = -\frac{\dot{p}_{\mathrm{bb}}(t)}{\ddot{\omega}_{\mathrm{bb}}(t)}\ , \tag{5.5}$$

where, $\dot{p}_{\mathrm{bb}}(t)$ can be obtained through the RoCoP estimation method presented in Chapter 4; and, according to FDF [34], the internal frequency of the device ω_{bb} can always be obtained through:

$$\omega_{\mathrm{bb}}(t) = \omega_{\mathrm{B}}(t) - x_{\mathrm{eq}}\,\dot{p}_{\mathrm{bb}}(t)\ , \tag{5.6}$$

where ω_{B} is the frequency at the bus the device is connected to, and x_{eq} is the equivalent impedance of the device.

Although (5.5) is, in general, fast and accurate, it may fail due to numerical issues. Equation (5.5), in fact, utilizes the second derivatives of the frequency signal as the denominator, which might change sign and, thus, cross zero in the first seconds after a contingency and therefore lead to a singularity of (5.5).

A simple heuristic solution to remove the singularity consists in holding the current value of the estimated inertia if the denominator is close to zero:

$$M^*_{\mathrm{bb}}(t) = \begin{cases} -\dfrac{\dot{p}_{\mathrm{bb}}(t)}{\ddot{\omega}_{\mathrm{bb}}(t)}, & |\ddot{\omega}_{\mathrm{bb}}| \geq \epsilon_o \ , \\ M^*_{\mathrm{bb}}(t-\Delta t)\,, & |\ddot{\omega}_{\mathrm{bb}}| < \epsilon_o \ , \end{cases} \tag{5.7}$$

where Δt is the sampling time and ϵ_o is a positive threshold to avoid the numerical issue. In the remainder of this chapter, we use (5.7), rather than (5.5), to compare the inertia estimation technique proposed in this deliverable with the one discussed in [41]. A large ϵ_o leads to estimation error, while a small ϵ_o cannot avoid numerical issues. According to a comprehensive set of numerical tests, we have concluded that a proper ϵ_o is hard to find, if it exists at all, and is device dependent. Therefore, in the following section, we propose a new formula with enhanced numerical stability.

5.4 Formula with Improved Numerical Stability

As discussed in Section 5.3, the fragile numerical stability of (5.5) is due to the division by $\ddot{\omega}$. Therefore, we propose the following differential equation that avoids such a division:

$$T_M \dot{M}^*_{\mathrm{bb}}(t) = \gamma\big(\ddot{\omega}(t)_{\mathrm{bb}}\big)\,\big(\dot{p}_{\mathrm{bb}}(t) + M^*_{\mathrm{bb}}\ddot{\omega}_{\mathrm{bb}}(t)\big)\ , \tag{5.8}$$

where

$$\gamma(x) = \begin{cases} -1\,, & x \geq \epsilon_x\,, \\ 0\,, & -\epsilon_x < x < \epsilon_x\,, \\ 1\,, & x \leq -\epsilon_x\,, \end{cases} \tag{5.9}$$

and ϵ_x is a small positive threshold closing to zero. The rationale behind (5.8) is as follows. At the equilibrium point, $M^*_{\mathrm{bb}}\ddot{\omega}_{\mathrm{bb}} = -\dot{p}_{\mathrm{bb}}$. According to (5.5), this conditions is obtained for $M^*_{\mathrm{bb}} = M_{\mathrm{bb}}$, which is the sought inertia value. During a transient, $M^*_{\mathrm{bb}}\ddot{\omega}_{\mathrm{bb}} \neq -\dot{p}_{\mathrm{bb}}$. Let us consider the case $M^*_{\mathrm{bb}}\ddot{\omega}_{\mathrm{bb}} > -\dot{p}_{\mathrm{bb}}$. Then the sign of $\dot{M}^*_{\mathrm{bb}}$ is adjusted through the function $\gamma(\ddot{\omega}_{\mathrm{bb}})$ in roder to make M^*_{bb} converge to M_{bb}. The sign of γ is decided based on the sign of $\ddot{\omega}_{\mathrm{bb}}$. If $\ddot{\omega}_{\mathrm{bb}} > 0$, M^*_{bb} has to decrease to decrease $M^*_{\mathrm{bb}}\ddot{\omega}_{\mathrm{bb}}$ and thus $\gamma(\ddot{\omega}_{\mathrm{bb}}) = -1$. Otherwise, if $\ddot{\omega}_{\mathrm{bb}} < 0$, $\gamma(\ddot{\omega}_{\mathrm{bb}}) = 1$ to increase M^*_{bb}. The time constant T_M decides the rate of change speed of M^*_{bb}. To avoid chattering around the the equilibrium point, a small deadband is included in (5.9), namely $(-\epsilon_x, \epsilon_x)$. A proper choice of ϵ_x can effectively reduce the impact of frequency fluctuations and noise, and therefore, the deadband for RoCoP, namely (5.4) is no longer needed.

Compared to (5.5), the inertia estimation formula (5.8) not only avoids numerical issues, but also allows filtering spikes and noises by adjusting T_M. Using a proper initial guess on M^*_{bb} can improve the speed of the estimation (5.8), but it is not essential for convergence. Finally, note that all results presented in this chapter are obtained assuming the initial condition $M^*_{\mathrm{bb}}(0) = 0$, where $t = 0$ s corresponds to the time at which the contingency occurs. This value serves to show that the proposed method is fast, effective and is suitable for on-line applications as it does not require storing historical data. In practice, however, any value of M^*_{bb} as obtained from previous estimations can be used.

5.5 Formula with Estimation of Damping

This section presents an inertia estimation formula that accounts for damping and PFC, which can also be utilized to estimate the droop gain of the FFR control of non-synchronous devices.

We first focus exclusively on SMs. The accuracy of (5.8) can be increased by removing the assumption $D_{\mathrm{G}} \approx 0$. With this in mind, we rewrite (5.8) as:

$$T_M \dot{M}^*_{\mathrm{G}}(t) = \gamma(\ddot{\omega}_{\mathrm{G}})\,[\,\dot{p}_{\mathrm{G}}(t) + M^*_{\mathrm{G}}\ddot{\omega}_{\mathrm{G}}(t) + D^*_{\mathrm{G}}\dot{\omega}_{\mathrm{G}}(t)\,]\ , \tag{5.10}$$

where D^*_{G} is the estimated value of damping, which is not known. The following equation allows estimating the damping:

$$T_D \dot{D}^*_{\mathrm{G}}(t) = \gamma\big(\Delta\omega_{\mathrm{G}}(t)\big)\,[\Delta p_{\mathrm{G}}(t) + M^*_{\mathrm{G}}\dot{\omega}_{\mathrm{G}}(t) + D^*_{\mathrm{G}}\Delta\omega_{\mathrm{G}}(t)]\ , \tag{5.11}$$

where $\Delta\omega_{\mathrm{G}}(t) = \omega_{\mathrm{G}}(t) - \omega_{\mathrm{G},o}$, with $\omega_{\mathrm{G},o} = \omega_{\mathrm{G}}(0)$. According to (5.9), the proposed inertia estimation formulas (5.10)-(5.11) introduce two thresholds related to the frequency variations of the device, namely $\epsilon_{\ddot{\omega}_{\mathrm{G}}}$ and $\epsilon_{\Delta\omega_{\mathrm{G}}}$. If properly set, these two thresholds can remove small frequency fluctuations resulting from the stochastic RESs in a more effective way than (5.4).

The on-line estimator based on (5.10)-(5.11) allows to eliminate the impact of damping on the accuracy of inertia estimation. However, the estimated damping D^*_{G} may never converge to the actual D_{G} due to the effect of PFC. In fact, D^*_{G} in (5.10) and (5.11) actually tracks $D_{\mathrm{G}} + R$ [72]. Since $\dot{\omega}_{\mathrm{G}}$ varies much slower than $\ddot{\omega}_{\mathrm{G}}$ within the first seconds after a contingency, D^*_{G} will take more time to converge than M^*_{G}. This discussion indicates that D^*_{G} cannot accurately estimate the damping of SMs but effectively improve the accuracy of inertia estimation by eliminating the impact of damping and PFC by taking their resulting power variations into account.

Equations (5.10)-(5.11) can be generalized for any device that regulates the frequency. Dropping for simplicity the subindex G, we have:

$$T_M \dot{M}^*(t) = \gamma(\ddot{\omega})[\,\dot{p} - M^*\ddot{\omega}(t) - D^*\dot{\omega}(t)\,], \tag{5.12}$$

$$T_D \dot{D}^*(t) = \gamma\left(\int \dot{\omega}dt\right)\left[\int \dot{p}(t)dt - M^*\dot{\omega}(t) - D^*\int \dot{\omega}(t)dt\right], \tag{5.13}$$

where ω is the internal frequency of the non-synchronous device. Note that the time constants T_M and T_D should be small enough to accurately track the time-varying inertia. Small time constants, however, make (5.12)-(5.13) more sensitive to noise and may introduce spurious oscillations. This issue can be solved through an additional filter.

The formulas (5.12)-(5.13) can be utilized to obtain the droop gain of the FFR that is modeled as:

$$p_{\mathrm{FFR}} = -R(\omega_{\mathrm{grid}} - \omega_{\mathrm{ref}}), \tag{5.14}$$

where ω_{grid} is the grid frequency.

Here we should highlight that in contrast to SMs, the primary response in CIG is instant along with the inertia response after the contingency. The damping is the friction of the rotational change of the device to the grid frequency, while the droop is the frequency deviation of the grid frequency to the nominal one. Since in CIG the device tracks the grid frequency change simultaneously, e.g. via the PLL with time constant below 0.1 s, we can deduce that D^* of the estimator (5.12)-(5.13), for CIG sources, actually tracks R [72].

5.6 Design of Real-Time Loop

This section provides the design of the inertia estimators based on the proposed formulas.

The proposed inertia estimation formulas can be used to fulfill the real-time measuring of the inertia through the estimators fed by the RoCoP and RoCoF signals.

Figure 11 shows the structure of a real-time inertia estimator based on (5.8). If $|\ddot{\omega}(t)| < \epsilon_{\ddot{\omega}}$ in $\gamma(\ddot{\omega})$ (see (5.9)), $dM^* = 0$ holds. This condition indicates that the estimated M^* can be held after the inertial response with a proper $\epsilon_{\ddot{\omega}}$.

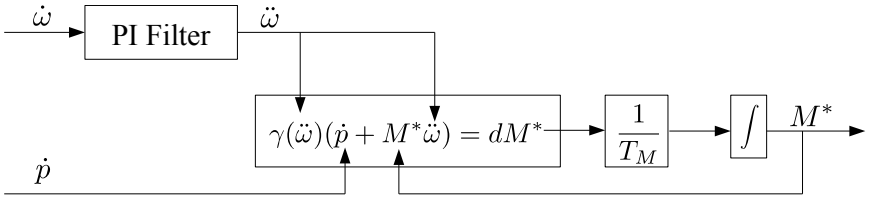

Figure 11 – Real-time loop for inertia estimation (5.8)

The control scheme of the PI filter included in Figure 11 is shown by Figure 12. The parameters of the PI filter are selected as $K_p = 50$, $K_i = 1$ and $T_f = 0.0001$ s for all simulation results of this chapter.

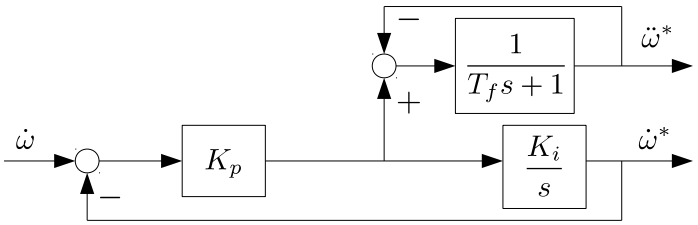

Figure 12 – Control scheme of PI filter

The real-time loop of the inertia estimator based on (5.12)-(5.13) is shown in Figure 13. Instead of directly taking the input $\dot{\omega}$ for computing dD^*, the $\dot{\omega}^*$ passing through the PI filter improves the robustness of the estimator against measurement noise.

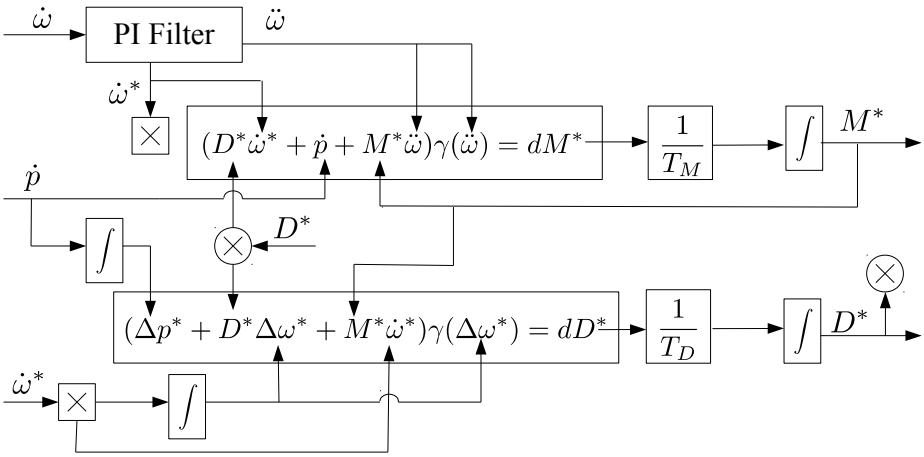

Figure 13 – Real-time loop for inertia estimation (5.12)-(5.13)

5.7 Simulation Results

The presented online inertia estimation approach is tested by considering Use Case FC_E.1 defined in deliverable D2.1.

6. Conclusions

This deliverable presents the frequency control algorithms developed for current VPPs in large scale deployment, including centralized PFC, SFC, frequency regulation metering, and a measurement-based technique to estimate the amount of frequency regulation provided by grid-connected devices, as well as an on-line inertia estimation for FFR.

Results indicate that the VPPs that coordinate the control of ESS and DERs shows a better frequency response when compared to a non-coordinated control scheme. Simulations also indicate that delays of different communication networks have a small impact on the transient response, which suggests that the coordinated control is feasible and its technology does not necessarily impact on the dynamic performance of the VPP.

Then, the deliverable proposes a coordinated control method of VPP to improve power system short-term transient frequency response. The proposed strategy is based on a coordinated control of DERs and ESSs in the VPP. A variety of control modes are compared and validated through Monte Carlo simulations. The impact of communication delays, stochastic processes as well as of the capacity of ESS on the overall transient behavior are also outlined. Based on the simulation results, the following conclusions can be drawn. First, the proposed coordinated control approach for ESS and DERs in VPP can significantly improve power system frequency stability. The proposed control approach performs better than either conventional VPPs that do not regulate the frequency, i.e. utilize a constant power set-point, and VPPs that regulate the frequency through the independent controllers of ESSs and DERs. Second, communication delays have a significant impact on the proposed coordinated control approach. This is as expected, since the proposed strategy works as a sort of *fast* secondary frequency control. To reduce the negative impact of communication networks without increasing the bandwidth, a two-phase coordinated control is proposed. In this operating mode, the ESS acts first whereas DERs are included in the coordinated control in a second phase. This reduces the impact of the limited capacity of the ESS and, in turn, improves the transient stability.

The deliverable also studies the impact of a linear aggregate operation of DERs on the dynamic response of a transmission system. With this aim, two approaches are considered, namely, an optimization problem based on MILP and an AGC that coordinates the DERs to achieve a linear ramping. Both approaches are simulated through a co-simulation platform. The case study shows that at a low penetration level of VPPs (5%) there is effectively no relevant difference on the dynamic performance of the system when imposing the ramping limit. For a higher penetration level of VPPs (20%), while frequency variations remain relatively small, imposing the ramping limit leads to a slightly better dynamic behavior of the system. A comparison of both approaches with respect to long-term frequency deviations shows that an AGC is to be preferred compared to scheduling based on an optimization problem as it leads to lower frequency variations.

Moreover, starting from the well-known dc power flow formulation, an alternative formulation of the FDF and a derivation of the link between the RoCoP injected into buses and bus frequency deviations are presented in the deriverable. Then, an empirical criterion to distinguish between devices that modify the frequency from those who do not is based on the RoCoP is provided. This requires the definition of a threshold determined based on the statistical properties of the device to be monitored. The proposed criterion can be utilized to properly reward the ancillary services of synchronous and non-synchronous devices that provide PFC. Simulation results confirm the accuracy and the robustness of the proposed approach in understanding whether a grid-connected device provides frequency control and/or inertial response following a power imbalance. The proposed approach appears to have great potential for practical applications. The index and the ‘regulating power,’ in fact, can be calculated with measurements and data that are available to the TSOs. No confidential measurement or data have to be obtained from the monitored devices.

Furthermore, based on the aforementioned criterion, an approximated expression to evaluate, during a transient, the equivalent inertia of a device is provided, which can be utilized to quantify the inertial response provided by non-synchronous devices. The deliverable further elaborates on such

inertia estimation method and proposes two formulas. The first formula avoids potential numerical issues while being simple. This formula shows satisfactory accuracy for the inertia estimation of SMs. The second formula improve accuracy by eliminating the effect of damping and/or droop. This formula works better for non-synchronous devices, including time-varying inertia response and stochastic sources.

7. List of Tables

8. List of Figures

9. References

[1] J. Morales, A. Conejo, H. Madsen, P. Pinson, and M. Zugno, *Integrating Renewables in Electricity Markets: Operational Problems*. Springer, 2014.

[2] N. Ruiz, I. Cobelo, and J. Oyarzabal, "A direct load control model for virtual power plant management," *IEEE Transactions on Power Systems*, vol. 24, no. 2, pp. 959–966, 2009.

[3] Y. Liu, H. Xin, Z. Wang, and D. Gan, "Control of virtual power plant in microgrids: a coordinated approach based on photovoltaic systems and controllable loads," *IET Generation, Transmission & Distribution*, vol. 9, no. 10, pp. 921–928, 2015.

[4] W. Zhong, J. Chen, M. Liu, M. A. A. Murad, and F. Milano, "Coordinated control of virtual power plants to improve power system short-term dynamics," *Energies*, vol. 14, no. 4, 2021.

[5] W. Zhong, M. A. A. Murad, M. Liu, and F. Milano, "Impact of virtual power plants on power system short-term transient response," *Electric Power Systems Research*, vol. 189, p. 106609, 2020.

[6] A. Arestova and Y. Sidorkin, "The use of wind farms and virtual power plants for emergency control in the future smart super grids," in *Proceedings of 2011 6th International Forum on Strategic Technology*, vol. 1. IEEE, 2011, pp. 437–442.

[7] C. Murphy and A. Keane, "Local and remote estimations using fitted polynomials in distribution systems," *IEEE Transactions on Power Systems*, vol. 32, no. 4, pp. 3185–3194, 2016.

[8] W. Zhong, M. Liu, and F. Milano, "A co-simulation framework for power systems and communication networks," in *Proceedings of the IEEE PowerTech Conference*, 2019, pp. 1–6.

[9] F. Milano, "A Python-based software tool for power system analysis," in *Proceedings of the IEEE PES General Meeting*, Vancouver, BC, July 2013.

[10] G. F. Riley and T. R. Henderson, *The ns-3 Network Simulator*. Berlin, Heidelberg: Springer Berlin Heidelberg, 2010, pp. 15–34.

[11] D. Pudjianto, C. Ramsay, and G. Strbac, "Virtual power plant and system integration of distributed energy resources," *IET Renewable Power Generation*, vol. 1, no. 1, pp. 10–16, 2007.

[12] R. Quint, L. Dangelmaier, I. Green, D. Edelson, V. Ganugula, R. Kaneshiro, J. Pigeon, B. Quaintance, J. Riesz, and N. Stringer, "Transformation of the grid: The impact of distributed energy resources on bulk power systems," *IEEE Power and Energy Magazine*, vol. 17, no. 6, pp. 35–45, Nov 2019.

[13] S. Ghavidel, L. Li, J. Aghaei, T. Yu, and J. Zhu, "A review on the virtual power plant: Components and operation systems," in *IEEE International Conference on Power System Technology (POWERCON)*, Sep. 2016, pp. 1–6.

[14] EirGrid Group, "Tomorrow's Energy Scenarios 2017." [Online]. Available: http://www.eirgridgroup.com/site-files/library/EirGrid/EirGrid-Tomorrows-Energy-Scenarios-Report-2017.pdf

[15] EirGrid, "EirGrid Grid Code. Version 8," 2019. [Online]. Available: http://www.eirgridgroup.com/site-files/library/EirGrid/Grid-Code.pdf

[16] P. Beagon, M. D. Bustamante, M. T. Devine, S. Fennell, J. Grant-Peters, C. Hall, R. Hill, T. Kerci, and G. O'Keefe, "Optimal scheduling of distributed generation to achieve linear aggregate response," in *141 st European Study Group with Industry University College Dublin, Ireland, 25-29 June 2018*, 2018, available at: http://www.maths-in-industry.org/miis/758/.

[17] T. Kërçi, M. T. Devine, M. A. A. Murad, and F. Milano, "Impact of the aggregate response of distributed energy resources on power system dynamics," in *Proceedings of the IEEE PES General Meeting*. IEEE, 2020.

[18] P. Kundur, *Power System Stability and Control*. New York: McGraw-Hill, 1994.

[19] F. Milano, F. Dörfler, G. Hug, D. J. Hill, and G. Verbič, "Foundations and challenges of low-inertia systems (invited paper)," in *Proceedings of the Power Systems Computation Conference (PSCC)*, Dublin, Ireland, June 2018, pp. 1–25.

[20] G. Morales-España, J. M. Latorre, and A. Ramos, "Tight and compact milp formulation for the thermal unit commitment problem," *IEEE Transactions on Power Systems*, vol. 28, no. 4, pp. 4897–4908, Nov 2013.

[21] P. Palensky, A. A. Van Der Meer, C. D. Lopez, A. Joseph, and K. Pan, "Cosimulation of intelligent power systems: Fundamentals, software architecture, numerics, and coupling," *IEEE Industrial Electronics Magazine*, vol. 11, no. 1, pp. 34–50, Mar. 2017.

[22] T. Kërçi and F. Milano, "A framework to embed the unit commitment problem into time domain simulations," in *IEEE International Conference on Environment and Electrical Engineering*, June 2019, pp. 1–5.

[23] T. Kërçi, J. Giraldo, and F. Milano, "Analysis of the impact of sub-hourly unit commitment on power system dynamics," *International Journal of Electrical Power & Energy Systems*, vol. 119, p. 105819, 2020.

[24] F. Milano, *Power System Modelling and Scripting*. London: Springer, 2010.

[25] H. F. Illian, “Frequency control performance measurement and requirements,” Lawrence Berkeley National Laboratory, Berkeley, Tech. Rep. LBNL-4145E, 2010.

[26] C. S. Xue and M. Martinez, “Review of the recent frequency performance of the Eastern, Western and ERCOT interconnections,” Lawrence Berkeley National Laboratory, Berkeley, Tech. Rep. LBNL-4144E, 2010.

[27] J. H. Eto, J. Undrill, P. Mackin, R. Daschmans, B. Williams, B. Haney, R. Hunt, J. Ellis, H. Illian, C. Martinez, M. O’Malley, K. Coughlin, and K. Hamachi LaCommare, “Use of frequency response metrics to assess the planning and operating requirements for for reliable integration of variable renewable generation,” Lawrence Berkeley National Laboratory, Berkeley, Tech. Rep. LBNL-4145E, 2010.

[28] P. Du and Y. Makarov, “Using disturbance data to monitor primary frequency response for power system interconnections,” *IEEE Transactions on Power Systems*, vol. 29, no. 3, pp. 1431–1432, May 2014.

[29] P. Du and J. Matevosyan, “Forecast system inertia condition and its impact to integrate more renewables,” *IEEE Transactions on Smart Grid*, vol. 9, no. 2, pp. 1531–1533, Mar. 2018.

[30] P. Bhui, N. Senroy, A. K. Singh, and B. C. Pal, “Estimation of inherent governor dead-band and regulation using unscented Kalman filter,” *IEEE Transactions on Power Systems*, vol. 33, no. 4, pp. 3546–3558, July 2018.

[31] K. Samarakoon, J. Ekanayake, and N. Jenkins, “Investigation of domestic load control to provide primary frequency response using smart meters,” *IEEE Transactions on Smart Grid*, vol. 3, no. 1, pp. 282–292, Mar. 2012.

[32] F. Milano and Á. Ortega, “A method for evaluating frequency regulation in an electrical grid – Part I: Theory,” *IEEE Transactions on Power Systems*, vol. 36, no. 1, pp. 183–193, Jan. 2021.

[33] Á. Ortega and F. Milano, “A method for evaluating frequency regulation in an electrical grid – Part II: Applications to non-synchronous devices,” *IEEE Transactions on Power Systems*, vol. 36, no. 1, pp. 194–203, Jan. 2021.

[34] F. Milano and Á. Ortega, “Frequency divider,” *IEEE Transactions on Power Systems*, vol. 32, no. 2, pp. 1493–1501, Mar. 2017.

[35] B. Stott, J. Jardim, and O. Alsac, “DC power flow revisited,” *IEEE Transactions on Power Systems*, vol. 24, no. 3, pp. 1290–1300, Aug. 2009.

[36] F. Bouffard, F. D. Galiana, and A. J. Conejo, “Market-clearing with stochastic security-part I: formulation,” *IEEE Transactions on Power Systems*, vol. 20, no. 4, pp. 1818–1826, Nov. 2005.

[37] F. Milano and R. Zárate Miñano, “A systematic method to model power systems as stochastic differential algebraic equations,” *IEEE Transactions on Power Systems*, vol. 28, no. 4, pp. 4537–4544, Nov. 2013.

[38] EirGrid, SONI, “Quarterly wind dispatch down report user guide.” [Online]. Available: http://www.eirgridgroup.com

[39] R. Zárate Miñano and F. Milano, “Construction of SDE-based wind speed models with exponentially decaying autocorrelation,” *Renewable Energy*, vol. 94, pp. 186 – 196, 2016.

[40] A. Derviškadić, P. Romano, and M. Paolone, “Iterative-interpolated DFT for synchrophasor estimation: A single algorithm for P- and M-class compliant PMUs,” *IEEE Transactions on Instrumentation and Measurement*, vol. 67, no. 3, pp. 547–558, Mar. 2018.

[41] F. Milano, Á. Ortega, and A. J. Conejo, “Model-agnostic linear estimation of generator rotor speeds based on phasor measurement units,” *IEEE Transactions on Power Systems*, vol. 33, no. 6, pp. 7258–7268, Nov. 2018.

[42] G. M. Jónsdóttir, B. Hayes, and F. Milano, “Optimum data sampling frequency for short-term analysis of power systems with wind,” in *Proceedings of the IEEE PES General Meeting*, 2018, pp. 1–5.

[43] E. Castillo, A. S. Hadi, A. Conejo, and A. Fernández-Canteli, “A general method for local sensitivity analysis with application to regression models and other optimization problems,” *Technometrics*, vol. 46, no. 4, pp. 430–444, 2004.

[44] G. M. Jónsdóttir and F. Milano, “Modeling solar irradiance for short-term dynamic analysis of power systems,” in *Proceedings of the IEEE PES General Meeting*, 2019.

[45] G. M. Jónsdóttir and F. Milano, “Modeling of short-term tidal power fluctuations,” *IEEE Transactions on Sustainable Energy*, vol. 11, no. 4, pp. 2337–2344, 2020.

[46] M. Liu, I. Dassios, G. Tzounas, and F. Milano, “Stability analysis of power systems with inclusion of realistic-modeling WAMS delays,” *IEEE Transactions on Power Systems*, vol. 34, no. 1, pp. 627–636, Jan. 2019.

[47] S. Wang, J. Hu, X. Yuan, and L. Sun, “On inertial dynamics of virtual-synchronous-controlled dfig-based wind turbines,” *IEEE Transactions on Energy Conversion*, vol. 30, no. 4, pp. 1691–1702, 2015.

[48] J. Hu, S. Wang, W. Tang, and X. Xiong, “Full-capacity wind turbine with inertial support by adjusting phase-locked loop response,” *IET Renewable Power Generation*, vol. 11, no. 1, pp. 44–53, 2017.

[49] Ö. Göksu, R. Teodorescu, C. L. Bak, F. Iov, and P. C. Kjær, "Instability of wind turbine converters during current injection to low voltage grid faults and PLL frequency based stability solution," *IEEE Transactions on Power Systems*, vol. 29, no. 4, pp. 1683–1691, 2014.

[50] F. Bizzarri, A. Brambilla, and F. Milano, "Analytic and numerical study of tcsc devices: Unveiling the crucial role of phase-locked loops," *IEEE Transactions on Circuits and Systems - I: Regular Papers*, vol. 65, no. 6, pp. 1840–1849, 2018.

[51] P. Romano and M. Paolone, "Enhanced interpolated-dft for synchrophasor estimation in FPGAs: Theory, implementation, and validation of a PMU prototype," *IEEE Transactions on Instrumentation and Measurement*, vol. 63, no. 12, pp. 2824–2836, 2014.

[52] G. Frigo, A. Derviškadić, Y. Zuo, and M. Paolone, "PMU-based ROCOF measurements: Uncertainty limits and metrological significance in power system applications," *IEEE Transactions on Instrumentation and Measurement*, vol. 68, no. 10, pp. 3810–3822, 2019.

[53] H. Gu, R. Yan, and T. K. Saha, "Minimum synchronous inertia requirement of renewable power systems," *IEEE Transactions on Power Systems*, vol. 33, no. 2, pp. 1533–1543, 2018.

[54] S. D'Arco, J. A. Suul, and O. B. Fosso, "A virtual synchronous machine implementation for distributed control of power converters in smartgrids," *Electric Power Systems Research*, vol. 122, pp. 180 – 197, 2015.

[55] E. Muljadi, V. Gevorgian, M. Singh, and S. Santoso, "Understanding inertial and frequency response of wind power plants," in *IEEE Power Electronics and Machines in Wind Applications*, 2012, pp. 1–8.

[56] G. S. Misyris, S. Chatzivasileiadis, and T. Weckesser, "Robust frequency control for varying inertia power systems," in *Proceedings of the IEEE PES Innovative Smart Grid Technologies Europe (ISGT Europe)*, 2018, pp. 1–6.

[57] J. Chen, M. Liu, F. Milano, and T. O'Donnell, "Adaptive virtual synchronous generator considering converter and storage capacity limits," *CSEE Journal of Power and Energy Systems*, accepted in June 2020, in press.

[58] K. Liu and Z. Q. Zhu, "Mechanical parameter estimation of permanent-magnet synchronous machines with aiding from estimation of rotor pm flux linkage," *IEEE Trans. on Industry Applications*, vol. 51, no. 4, pp. 3115–3125, 2015.

[59] P. M. Ashton, C. S. Saunders, G. A. Taylor, A. M. Carter, and M. E. Bradley, "Inertia estimation of the gb power system using synchrophasor measurements," *IEEE Transactions on Power Systems*, vol. 30, no. 2, pp. 701–709, 2015.

[60] P. M. Ashton, G. A. Taylor, A. M. Carter, M. E. Bradley, and W. Hung, "Application of phasor measurement units to estimate power system inertial frequency response," in *Proceedings of the IEEE PES General Meeting*, 2013, pp. 1–5.

[61] Á. G. González Rodríguez, A. González Rodríguez, and M. Burgos Payán, "Estimating wind turbines mechanical constants," in *Int. Conf. on Renewable Energy and Power Quality (ICREPQ)*, Sevilla, March 2007, p. 6977045.

[62] D. P. Chassin, Z. Huang, M. K. Donnelly, C. Hassler, E. Ramirez, and C. Ray, "Estimation of wecc system inertia using observed frequency transients," *IEEE Transactions on Power Systems*, vol. 20, no. 2, pp. 1190–1192, 2005.

[63] A. Fernández Guillamón, A. Vigueras Rodríguez, and Á. Molina García, "Analysis of power system inertia estimation in high wind power plant integration scenarios," *IET Renewable Power Generation*, vol. 13, no. 15, pp. 2807–2816, 2019.

[64] P. Wall, P. Regulski, Z. Rusidovic, and V. Terzija, "Inertia estimation using PMUs in a laboratory," in *Proceedings of the IEEE PES Innovative Smart Grid Technologies Europe (ISGT Europe)*, 2014, pp. 1–6.

[65] V. Terzija, G. Valverde, D. Cai, P. Regulski, V. Madani, J. Fitch, S. Skok, M. M. Begovic, and A. Phadke, "Wide-area monitoring, protection, and control of future electric power networks," *Proceedings of the IEEE*, vol. 99, no. 1, pp. 80–93, Jan 2011.

[66] N. Petra, C. G. Petra, Z. Zhang, E. M. Constantinescu, and M. Anitescu, "A Bayesian approach for parameter estimation with uncertainty for dynamic power systems," *IEEE Transactions on Power Systems*, vol. 32, no. 4, pp. 2735–2743, 2017.

[67] J. Zhang and H. Xu, "Online identification of power system equivalent inertia constant," *IEEE Transactions on Industrial Electronics*, vol. 64, no. 10, pp. 8098–8107, 2017.

[68] R. K. Panda, A. Mohapatra, and S. C. Srivastava, "Application of indirect adaptive control philosophy for inertia estimation," in *2019 IEEE PES GTD Grand International Conference and Exposition Asia (GTD Asia)*, 2019, pp. 478–483.

[69] R. K. Panda, A. Mohapatra, and S. C. Srivastava, "Online estimation of system inertia in a power network utilizing synchrophasor measurements," *IEEE Transactions on Power Systems*, pp. 1–1, 2019.

[70] J. Schiffer, P. Aristidou, and R. Ortega, "Online estimation of power system inertia using dynamic regressor extension and mixing," *IEEE Transactions on Power Systems*, vol. 34, no. 6, pp. 4993–5001, 2019.

[71] T. Kerdphol, F. S. Rahman, M. Watanabe, Y. Mitani, D. Turschner, and H. Beck, "Enhanced virtual inertia control based on derivative technique to emulate simultaneous inertia and damping properties for microgrid frequency regulation," *IEEE Access*, vol. 7, pp. 14 422–14 433, 2019.

[72] M. Liu, J. Chen, and F. Milano, “On-line inertia estimation for synchronous and non-synchronous devices,” *IEEE Transactions on Power Systems*, 2020, pre-print available on ieeexplore.ieee.org.

[73] Gurobi Optimization, LLC, “Gurobi optimizer reference manual,” 2018. [Online]. Available: http://www.gurobi.com

[74] I. Abdur-Rahman, S. Niemeyer, and R. Vera, “Frequency regulation: Is your plant compliant?” *Power Engineering*, 2010, available at www.power-eng.com.

[75] Á. Ortega and F. Milano, “Modeling, simulation, and comparison of control techniques for energy storage systems,” *IEEE Transactions on Power Systems*, vol. 32, no. 3, pp. 2445–2454, May 2017.

[76] H. Zhao, Q. Wu, S. Huang, H. Zhang, Y. Liu, and Y. Xue, “Hierarchical control of thermostatically controlled loads for primary frequency support,” *IEEE Transactions on Smart Grid*, vol. 9, no. 4, pp. 2986–2998, 2018.

[77] F. Milano and Á. Ortega, *Frequency Variations in Power Systems: Modeling, State Estimation, and Control*. John Wiley & Sons, 2020.

[78] J. Chen, M. Liu, and T. O’Donnell, “Replacement of synchronous generator by virtual synchronous generator in the conventional power system,” in *Proceedings of the IEEE PES General Meeting*, Atlanta, GA, USA, 2019, pp. 1–5.

[79] Y. Pititeeraphab, T. Jusing, P. Chotikunnan, N. Thongpance, W. Lekdee, and A. Teerasoradech, “The effect of average filter for complementary filter and kalman filter based on measurement angle,” in *2016 9th Biomedical Engineering International Conference (BMEiCON)*, 2016, pp. 1–4.

[80] G. M. Jónsdóttir and F. Milano, “Data-based continuous wind speed models with arbitrary probability distribution and autocorrelation,” *Renewable Energy*, vol. 143, pp. 368–376, Dec. 2019.

[81] M. P. N. van Wesenbeeck, S. W. H. de Haan, P. Varela, and K. Visscher, “Grid tied converter with virtual kinetic storage,” in *Proceedings of the IEEE PowerTech Conference*, 2009, pp. 1–7.

10. List of Abbreviations

AGC	Automatic Generation Control
CIG	Converter Interfaced Generation
COI	Center-Of-Inertia
DER	Distributed Energy Resource
DFIG	Doubly-Fed Induction Generator
EMF	Electromotive Force
ESS	Energy Storage System
FDF	Frequency Divider Formula
FFR	Fast Frequency Response
GFC	Grid-Following Converter
KPI	Key Performance Indicator
LPF	Low-Pass Filter
MILP	Mixed-Integer Linear Programming
MPPT	Maximum Power point Tracking
PFC	Primary Frequency Control
PI	Proportional-Integral
PLL	Phase-Locked Loop
PMU	Phasor Measurement Unit
POC	Point of Connection
RES	Renewable Energy Source
RoCoF	Rate of Change of Frequency
RoCoP	Rate of Change of Power
RTU	Remote Terminal Unit
SFC	Secondary Frequency Control
SM	Synchronous Machine
SPV	Solar Photovoltaic
SRF-PLL	Synchronous Reference Frame Phase-Locked Loop
sSCUC	stochastic Security-Constrained Unit Commitment
TCL	Thermostatically-Controlled Load
TG	Turbine Governor
TSO	Transmission System Operator
ULTC	Under-Load Tap Changer
VPP	Virtual Power Plant

VSG Virtual Synchronous Generator

VSM Virtual Synchronous Machine

WPP Wind Power Plant

WSCC Western Systems Coordinating Council

WT Wind Turbine

ANNEX – Simulation Results

This ANNEX presents the simulation results on the techniques described in this deliverable. All results are obtained using the Python-based software tool Dome [9].

A.1 Coordinated VPP Control

This section presents simulation results on the coordinated VPP control strategy presented in Chapter 2.

A.1.1 Monte Carlo Analysis

We first discuss the robustness of the proposed control approach concerning perturbations such as a three-phase fault at bus 7 occurring at $t = 1$ s and cleared after 100 ms. The stochastic perturbations are the power variations of wind and solar power plants with respect to the forecast of wind speed/solar irradiance, and 15% of the loads in the whole system. For each mode, 500 Monte Carlo time domain simulations are solved. The trajectories of the frequencies for Modes 1 to 3 are shown in Figure 14. The trajectories of the frequency for Modes 4 to 6 with three different transfer functions $H(s)$ are shown in Figure 15. The considered transfer functions are proportional gain, PI controller and lead-lag controller. For all controllers, the parameters that lead to the best dynamic performance are selected through a trial-and-error approach. For simplicity, and since the size of all DERs and ESS is similar, $K_i = 1, \forall i = 1, \ldots, n$. Finally, Table 1 shows the mean frequency, μ_{COI}, as well as the standard deviation of the frequency σ_{COI}, calculated at $t = 50$ s, for the six control modes and the three transfer functions $H(s)$ considered in this case study.

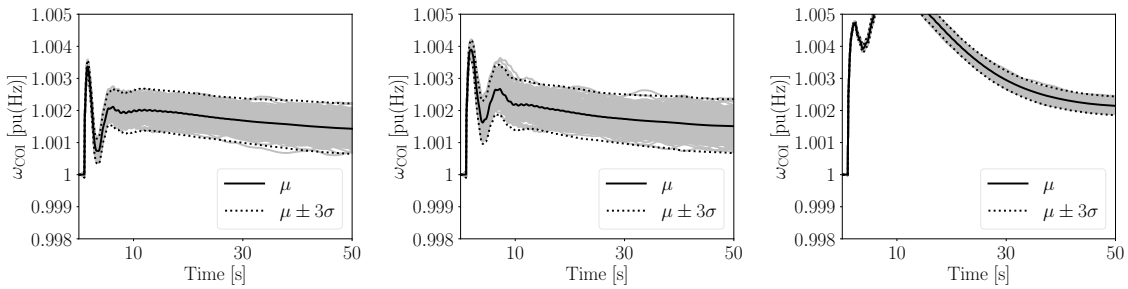

(a) Mode 1 **(b) Mode 2** **(c) Mode 3**

Figure 14 – Use Case FC_B.1 – COI frequency without the coordinated control

	Statistics	Mode 1	Mode 2	Mode 3
	μ_{COI}	1.001431	1.001511	1.002144
	$\sigma_{\text{COI}} \times 10^{-5}$ [pu(Hz)]	23.60	28.10	9.73
Control Type	Statistics	Mode 4	Mode 5	Mode 6
Proportional Control	μ_{COI} [pu(Hz)]	1.000328	1.000323	1.000321
	$\sigma_{\text{COI}} \times 10^{-5}$ [pu(Hz)]	1.83	1.58	1.43
Lead-Lag	μ_{COI} [pu(Hz)]	1.000198	1.000155	1.000135
	$\sigma_{\text{COI}} \times 10^{-5}$ [pu(Hz)]	8.62	2.24	3.27
PI	μ_{COI} [pu(Hz)]	1.000267	1.000020	1.000023
	$\sigma_{\text{COI}} \times 10^{-5}$ [pu(Hz)]	12.40	1.37	1.60

Table 1 – Use Case FC_B.1 – Statistics of different VPP control modes

The comparison of the trajectories shown in Figures 14 and 15 as well as of the results given in Table 1 indicates that the VPP control modes that include the proposed coordinated approach

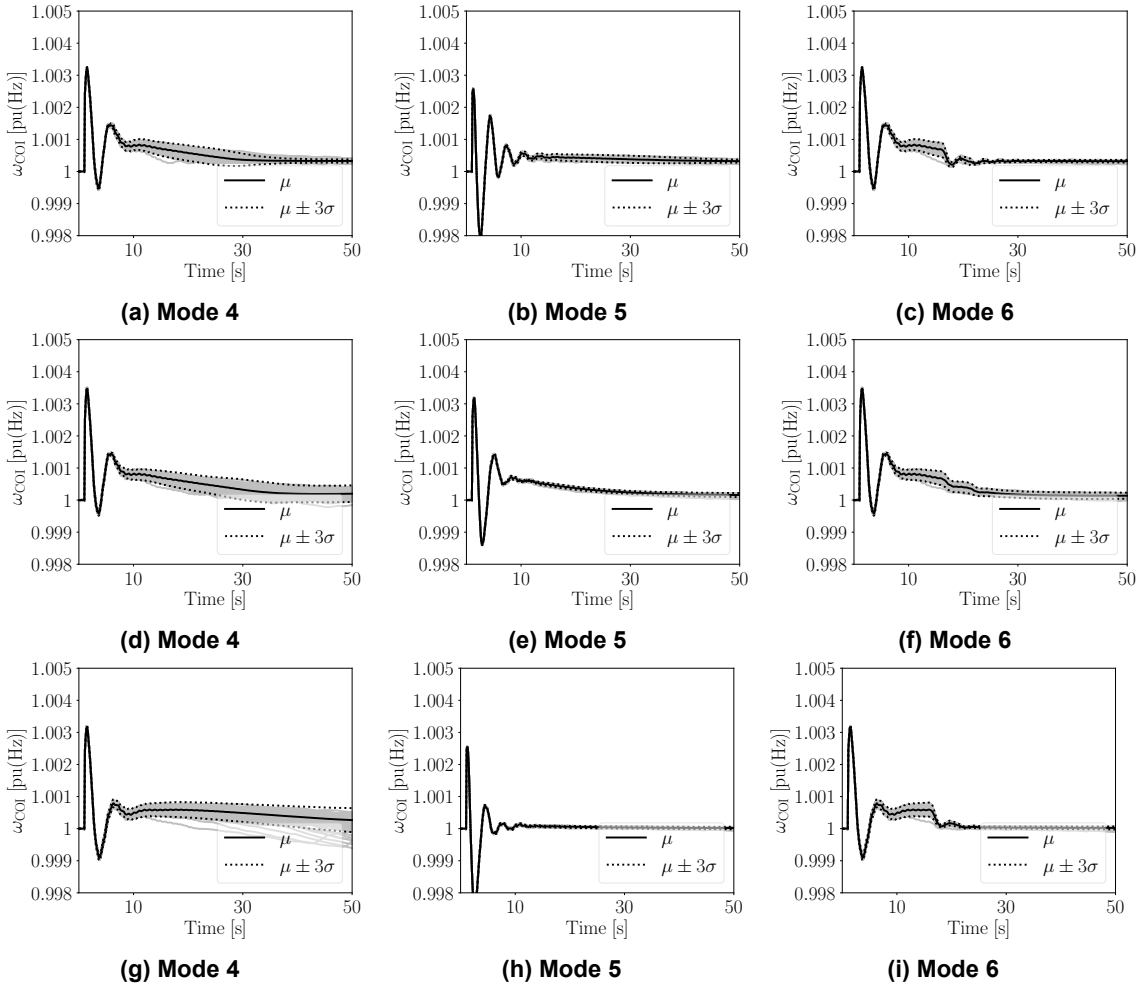

Figure 15 – Use Case FC_B.1 – COI frequency using: (a)-(c) proportional gain; (d)-(f) lead-lag; and (g)-(i) PI control

control (Modes 4-6) have an overall better performance than the strategies with no coordination (Modes 1-3).

It is interesting to note that, for Mode 4 (see Figures 15a, 15d and 15g), the standard deviation slightly increases for $10 < t < 30$ s because the ESS is running at its maximum output and thus loses its capability to regulate the frequency. In Mode 5, coordinating the DERs to provide extra frequency support can help solve this problem as shown in Figures 15b, 15e and 15h. However, this leads to a larger frequency deviation during the initial transients ($0 < t < 10$ s). Finally, Mode 6, in which a timer is utilized to delay the action of DERs, shows the best dynamic performance (see Figures 15c, 15f and 15i).

The results shown in Figure 15 are obtained with optimal settings for each controller. For the PI controller, a small dead-band is included in the frequency deviation signal $\Delta\omega_{\mathrm{POC}}$. While all controllers perform well, they have different performances depending on the mode. The PI controller performs best if both ESS and DERs regulate the frequency. However, if only the ESS is utilized to regulate the frequency, the PI controller leads more often the ESS to its maximum power output, thus making the control less efficient as compared to the proportional and lead-lag controllers. All controllers perform well for Mode 6, i.e. when a timer shifts the action of the DERs. The timer, in fact, exploits the ability of the ESS to regulate the frequency in the first seconds but avoids ESS saturations in the longer term.

A.1.2 Impact of Communication Delays

There exists a delay when the frequency signal $\Delta\omega_{\mathrm{POC}}$ and active power p_{inj} are transmitted through the communication network. In this section, the communication delay in three levels of communication networks, namely, high-speed, middle-speed, and low-speed network is considered. All remote signals are considered as 100 bytes PMU data with a reporting rate of 25 frames per second. UDP/IP protocol is adopted to avoid data re-transmission thus reducing the communication delay, where the physical link layer of the communication network is a point-to-point link. The background traffic consists of both 500 bytes Remote Terminal Unit (RTU) data with a reporting rate of 2 frames per second, and 1024 bytes video streams with a reporting rate of 200 frames per second, respectively. Table 2 shows the parameters of each communication network considered.

Levels	Bandwidth	PMU Data Rate	Background Traffic
High Speed	20 Mbps	25 frames/s	RTU, Video Stream
Medium Speed	5 Mbps	25 frames/s	RTU, Video Stream
Low Speed	1 Mbps	25 frames/s	N/A

Table 2 – Use Case FC_B.1 – Parameters of the communication networks

Most real-world communication networks utilized in power system applications are somewhere in between the high-speed and medium-speed communication networks depicted in Table 2. However, low-bandwidth communication networks are cheaper and, thus, the low-speed communication network is also considered here. Clearly, the lower the speed (bandwidth) of the communication network, the higher the delays of the control signals.

Figure 16 shows the impact of communication delays on the Center-Of-Inertia (COI) frequency as obtained with the three communication networks of Table 2. The system undergoes the same three-phase fault considered in Section A.1.1. Only Modes 4, 5 and 6 are compared as these are the modes that require a communication network. Simulation results, which were obtained using the proportional controller, indicate that the proposed coordinated control approach, especially Modes 5 and 6 are particularly impacted by communication delays.

When the communication network has a low bandwidth with a large time-varying delay of around 200 ms, the approach that only coordinates the ESS gives rise to a frequency oscillation (see the interval between 25 and 35 s in Figure 16a). Mode 6 sharply increases this oscillation. Then in the medium-speed communication network with a medium time-varying delay of around 100 ms, the performances for Modes 4 and 6 are acceptable, however, for Mode 5, the frequency oscillation is still significant. Finally, the delays of the high-speed communication network are around 55 ms. This delay has only a slight impact on the overall frequency behavior. Based on the simulation results, it appears, thus, that communication delays should be kept below 100 ms when the proposed coordinated control approach is adopted.

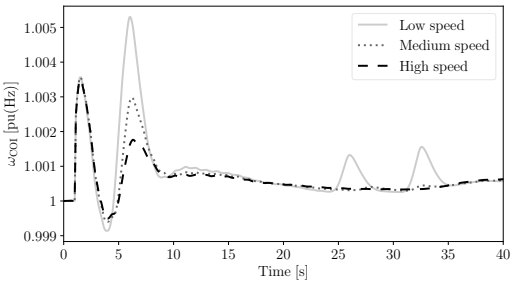

(a) Mode 4

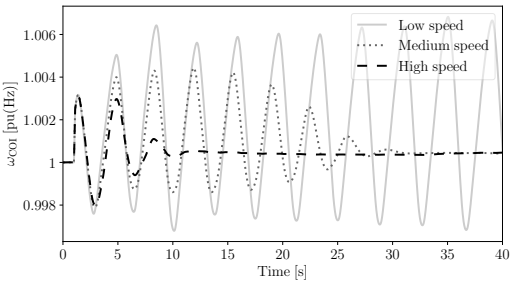

(b) Mode 5

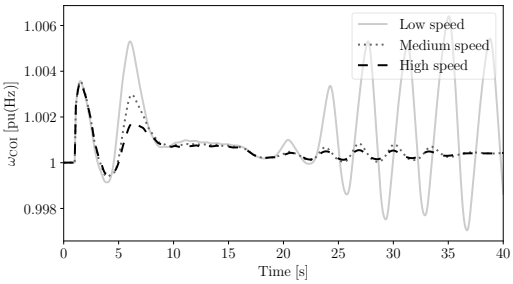

(c) Mode 6

Figure 16 – Use Case FC_B.1 – COI frequency following a three-phase fault. Measured signals are transmitted through high/medium/low speed communication networks

A.2 Automatic Generation Control of VPPs

This section presents simulation results on AGC-based VPP described in Chapter 3. The focus of the study is on the first 15 minutes of the planning horizon that is the relevant time window for the aggregated response of DERs. The time period t used in the simulations is 1 minute. The study carries out Monte Carlo time domain simulations and 50 simulations are solved for each case considered. For the sake of comparison, results are also obtained with the MILP model proposed in [16] and are used as a reference. The MILP problem and the sub-hourly sSCUC model are implemented in Python and solved using Gurobi [73], while simulation results are obtained using Dome. The modeling of wind power uncertainty and volatility within the sub-hourly sSCUC model is the same as in [23].

A.2.1 MILP-based VPP With Ramping Constraints

With the MILP-based VPP in operation, Figure 17 depicts the trajectories of the frequency of the COI (ω_{COI}) with the ramping limit enforced. As it can be seen, there are significant frequency oscillations at the beginning of the planning horizon due to the ramping of generators. The value of the standard deviation of the frequency is $\sigma_{\text{COI}} = 0.000571$ pu(Hz).

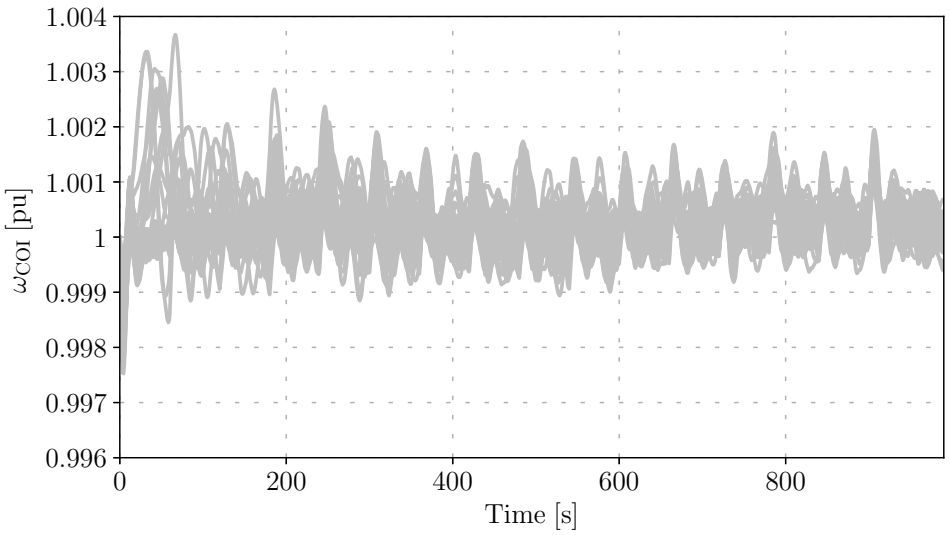

Figure 17 – Use Case FC_B.2 – COI frequency for MILP-based VPP with ramping constraint

A.2.2 MILP-based VPP Without Ramping Constraints

We discuss the effect of the ramping limit enforced by the TSO to the VPP on the dynamic behavior of the system. Figure 18 shows the trajectories of the ω_{COI} for the case when the ramping limit is not enforced. This leads to a worse dynamic behavior of the system compared to Figure 17. In this case, $\sigma_{\text{COI}} = 0.000645$ pu(Hz). Note that, using the same simulation setup, it was shown in [17] that for a lower level of VPP penetration, i.e. 5%, the impact of the ramping limit on the frequency deviations is smaller. Hence, increasing the penetration levels of VPPs also increases the impact of ramping limits. On the other hand, such impact does not seem to constitute a stability issue for the system.

A.2.3 AGC-Based VPP

We discuss the performance of the AGC described in Section 3.2. The gain of the AGC is set to $K_0 = 50$. Figure 19 shows the trajectories of the frequency of the COI ω_{COI} for 15 minutes. The frequency variations are significantly lower, i.e. $\sigma_{\text{COI}} = 0.000459$ pu(Hz), compared to those shown

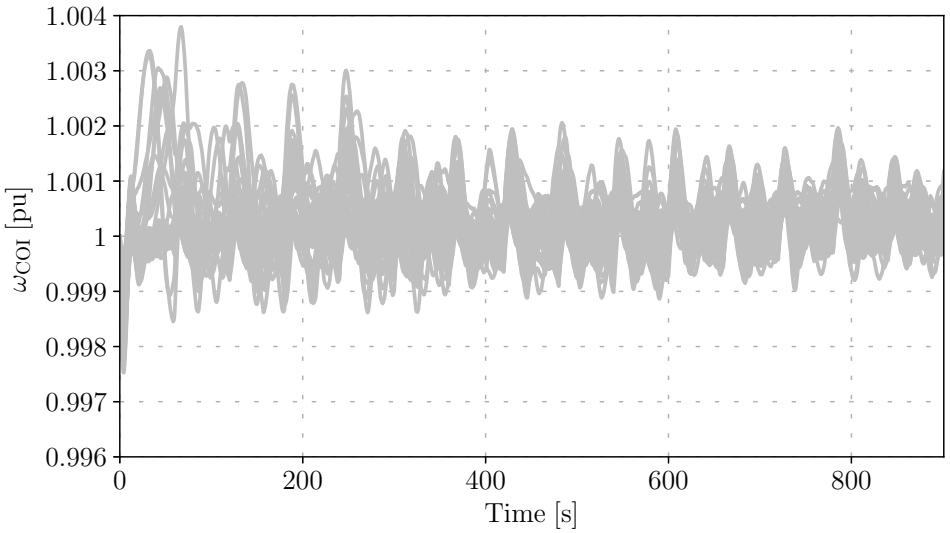

Figure 18 – Use Case FC_B.2 – COI frequency for MILP-based VPP without ramping constraint

in Figures 17 and 18. This is due to the fact that the AGC coordinates the DERs in such a way that they start ramping up all at the same time and then smoothly increase their generation (see Figure 20). Thus, from a system operator point of view, the AGC-based VPP is preferable compared to a conventional VPP scheduling based on the solution of a MILP problem.

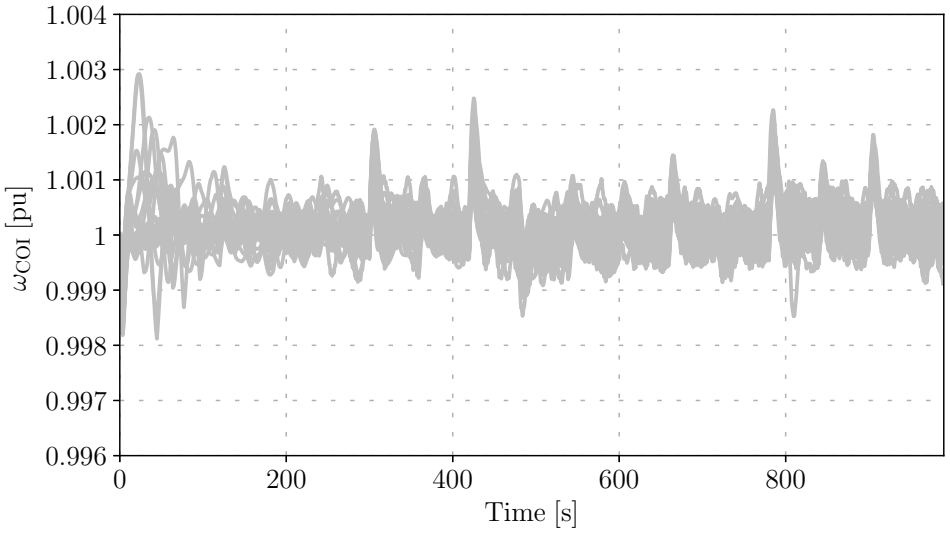

Figure 19 – Use Case FC_B.2 – COI frequency for AGC-based VPP

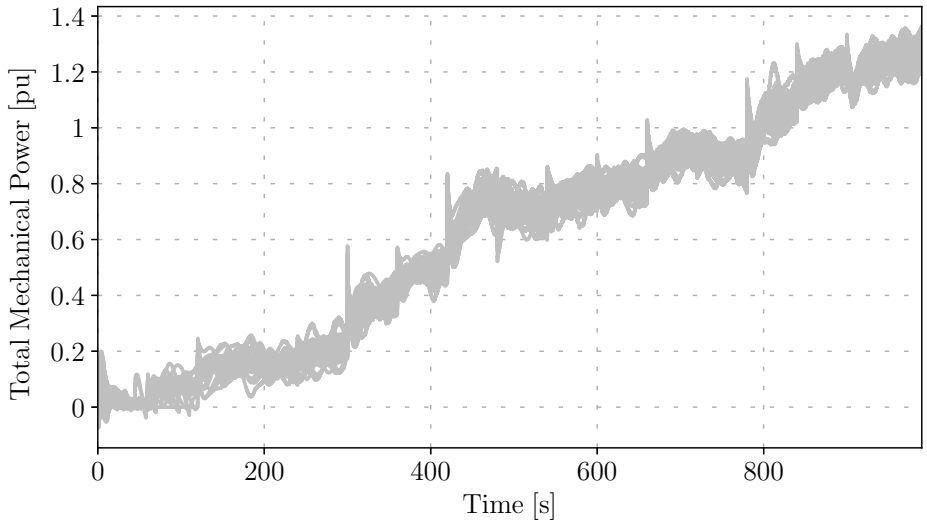

Figure 20 – Use Case FC_B.2 – Total mechanical power of the machines of the AGC-based VPP

A.3 Frequency Regulation Metering During Transients

This section presents simulation results on the RoCoP index proposed in Chapter 4 for metering frequency regulation provided by synchronous and non-synchronous devices in transient conditions.

A.3.1 Synchronous Machines

In this section, the modified WSCC system includes an AGC implemented as a perfect tracking integral controller.

1) Comparison with Loads: Figure 21 shows the RoCoP for the generator connected to bus 3 and the load connected to bus 8 following the outage of 20% of the load connected to bus 5. Dropping for simplicity the dependency on time, the RoCoP of buses 3 and 8 are given by the following expressions based on (4.15):

$$\begin{aligned} \dot{p}'_{\mathrm{B},3} &= 17.06\,\Delta\tilde{\omega}_{\mathrm{B},3} - 17.06\,\Delta\tilde{\omega}_{\mathrm{B},9} \\ \dot{p}'_{\mathrm{B},8} &= 23.48\,\Delta\tilde{\omega}_{\mathrm{B},8} - 13.7\,\Delta\tilde{\omega}_{\mathrm{B},7} - 9.784\,\Delta\tilde{\omega}_{\mathrm{B},9}\ , \end{aligned} \tag{A.1}$$

where the coefficients are obtained from $\mathbf{B}_{\mathrm{bus}}$ (see ANNEX in D2.1) and the symbol '$\sim$' on top of a bus frequency represents estimated values from the SRF-PLL. As thoroughly discussed in [41], for practical applications, if a measurement is not available, this can be calculated using measurements from other buses. For example, if there is no PMU at bus 3, $\Delta\tilde{\omega}_{\mathrm{B},3}$ can be replaced in (A.1) with:

$$\Delta\tilde{\omega}_{\mathrm{B},3} = \frac{32.43}{17.06}\,\Delta\tilde{\omega}_{\mathrm{B},9} - \frac{5.588}{17.06}\,\Delta\tilde{\omega}_{\mathrm{B},6} - \frac{9.784}{17.06}\,\Delta\tilde{\omega}_{\mathrm{B},8}, \tag{A.2}$$

which can be readily deduced from the last row of $\mathbf{B}_{\mathrm{bus}}$ (see ANNEX in D2.1).

Simulation results show that, as expected, at the generator bus, $\dot{p}'_{\mathrm{B},3}(t) \neq 0$ after the load outage, whereas, at the load bus, $\dot{p}'_{\mathrm{B},8}(t) \approx 0, \forall t$. The spike at the beginning of the simulation of the load bus is due to the numerical integration of the SRF-PLL, and does not represent any physical behavior of the system. In steady state, the index $\dot{p}'_{\mathrm{B},h}(t)$ is null, which indicates that, in stationary conditions, all machines rotate at the same speed and that all frequency controllers are inactive.

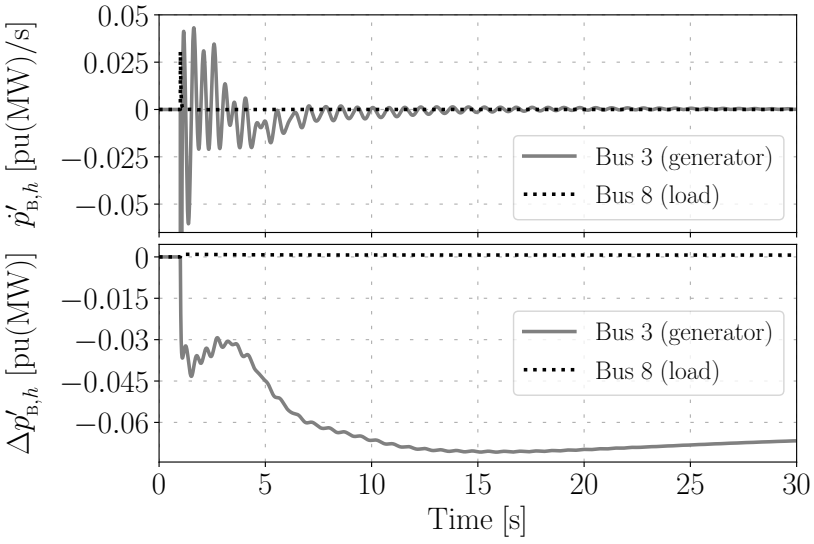

Figure 21 – Use Case FC_D.1 – RoCoP and estimated variations of power injection at buses 3 and 8

2) Layers of Frequency Control: Figure 22 shows the effect of removing the AGC from the system as well as the PFC from the generator at bus 3. The effect of the AGC on the RoCoP and the estimated power injection is negligible. This result is consistent with the transient nature of the RoCoP. On the other hand, if the PFC is disabled, the effect on the RoCoP is evident a few seconds after the

contingency. In the first instants, the response of the RoCoP is driven exclusively by the inertia of the machine, as the three trajectories are fairly similar up to about 2 seconds after the loss of the load. This property can be exploited to estimate accurately the inertia of the machines regardless of the type of frequency control to which the machines are coupled.

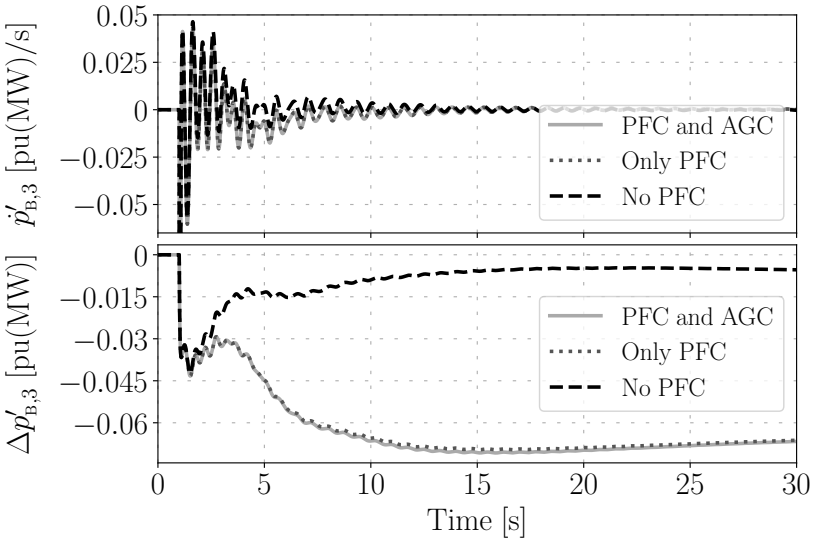

Figure 22 – Use Case FC_D.1 – RoCoP and estimated variations of power injection at generation bus 3 for various frequency controls

3) Actual vs Regulating Active Power Injection: The estimated power injection at bus 3 shown in the bottom panels of Figures 21 and 22 indicates that there is a jump in the trajectory of the active power generated by the SM. However, the turbine governors of SMs require several seconds to vary their mechanical power generation to match the power imbalance that, in this case, is due to the loss of part of the load at bus 5. This is graphically represented in Figure 23, where the estimated $\Delta p'_{\mathrm{B},3}(t)$ is compared with the variations of the actual active power generated by the SM at bus 3 for the cases without any frequency control, and with both PFC and SFC.

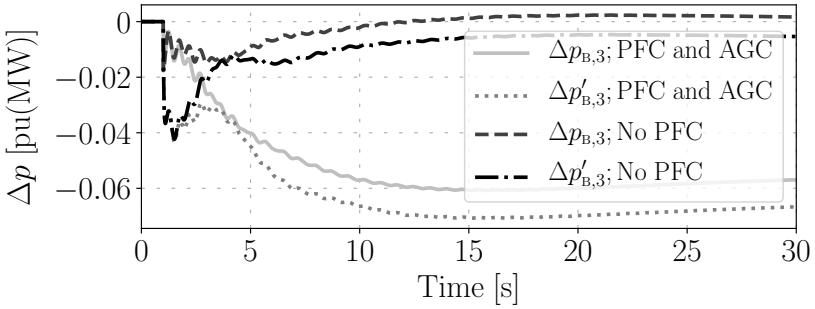

Figure 23 – Use Case FC_D.1 – Variations of the active power injected to bus 3 and regulating power for various frequency controls

Results shown in Figure 23 indicate that the estimated $\Delta p'_{\mathrm{B},3}(t)$ includes the effect of the (fast) inertial response of the machine, $M_{\mathrm{G}}\dot{\omega}_{\mathrm{G}}(t)$, and the PFC, $p_{\mathrm{PFC}}(t)$. In Figure 23, $\Delta p'_{\mathrm{B},3}(t)$ is calculated using (4.27), whereas the variation of the total power injection at the generator bus is $\Delta p_{\mathrm{B},3}(t) = p_{\mathrm{B},3}(t) - p_{\mathrm{B},3o}$. The actual variations of the mechanical power of the SM are smooth even in the first instants after the contingency, and following later a similar behavior than that estimated by the regulating power $\Delta p'_{\mathrm{B},3}(t)$, i.e. after the inertial response of the SM gives way to the PFC.

4) Impact of Deadbands in the TG*:* TGs of SMs usually include deadbands on their frequency error input signal to *minimize generator movement due to frequency regulation* [74]. Inclusion of this deadband results in a reduction of the sensitivity of the PFC on imbalances in the system, thus impacting on the variations of the power injected by the generators after a disturbance. Usually,

the value of the deadband is designed to neglect *small* frequency variations due to, e.g., small load fluctuations or generation variability of renewable sources, and is of the order of a few tens of millihertzs.

For the sake of illustration, a deadband of 75 mHz (0.00125 pu) is considered in the example shown in Figure 24, where the case from the previous section with PFC and AGC is simulated. The inclusion of the deadband reduces the variations of active power injected by the SM. This reduction is properly captured by the estimated regulating power, indicating that the accuracy of the estimation is not affected by the inclusion of the deadband.

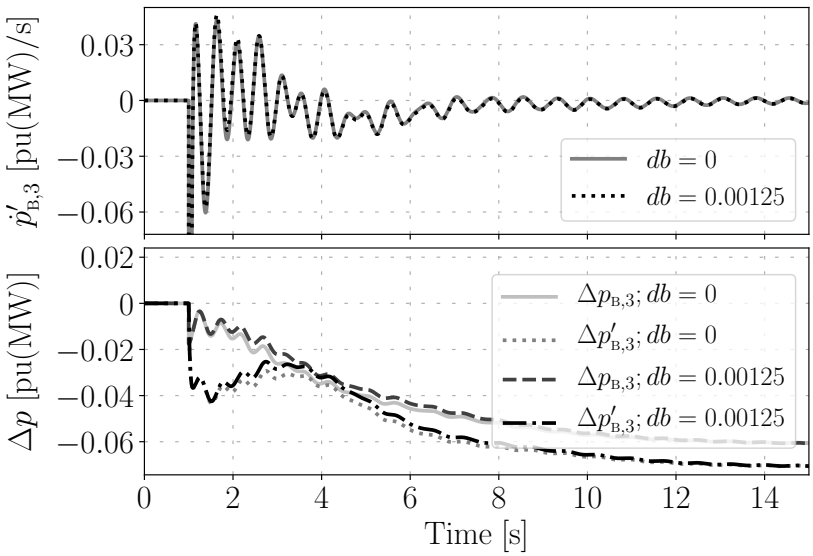

Figure 24 – Use Case FC_D.1 – RoCoP and variations of the active power injected to bus 3 and regulating power with and without deadband in the turbine governor input signal

5) Short-circuit Analysis: As already discussed, accurate measurements of the frequency are required for the practical application of the technique discussed in this section, which can pose some limitations, especially if fast events are registered such as short-circuits and line outages. This study considers the well-known and ubiquitous SRF-PLL for estimating the frequency at a specific bus based on the processing of the bus voltage phase angle. It is also well-known that SRF-PLLs are prone to numerical issues and thus to measurement inaccuracies if such a phase angle experiences sudden jumps due to, e.g., the fast events discussed above, as well as other phenomena such as signal noise. In this illustrative example, the accuracy of the proposed RoCoP is studied when the system faces a short-circuit, cleared by the opening of the faulted line.

In this example, a three-phase fault is simulated at bus 7, which is cleared after 70 ms by opening the line connecting buses 7 and 5. The RoCoP at buses 3 and 8 is shown at the top panel of Figure 25. The SRF-PLL causes spikes in the RoCoP which leads to peaks of $|\dot{p}'_{\mathrm{B},3}|_{\max} \approx 25$ and $|\dot{p}'_{\mathrm{B},8}|_{\max} \approx 100$. However, such spikes last for about the duration of the fault, i.e., around 100 ms. After such time, the RoCoP is able to accurately track the electromechanical oscillations of the machine, whereas it is virtually constant and equal to zero for the case of the load.

The small-amplitude oscillations of $\dot{p}'_{\mathrm{B},8}(t)$ in the first second after the fault clearance require a brief explanation. When the fault occurs and then when it is cleared, the bus voltage phase angles jump with different amplitudes at different buses. This means that the PLLs will recover an accurate estimation of the frequency with a lag that is different from bus to bus. The oscillations of $\dot{p}'_{\mathrm{B},8}(t)$ are thus due to the offset between the PLL frequency estimations at buses 7, 8 and 9 following the fault.

The bottom panel of Figure 25 shows the variations of the injected and regulating active power at bus 3. During the first seconds after the contingency, the dominant component of the regulating power is not the active power injected by the machine, but the machine inertia. This causes a drift

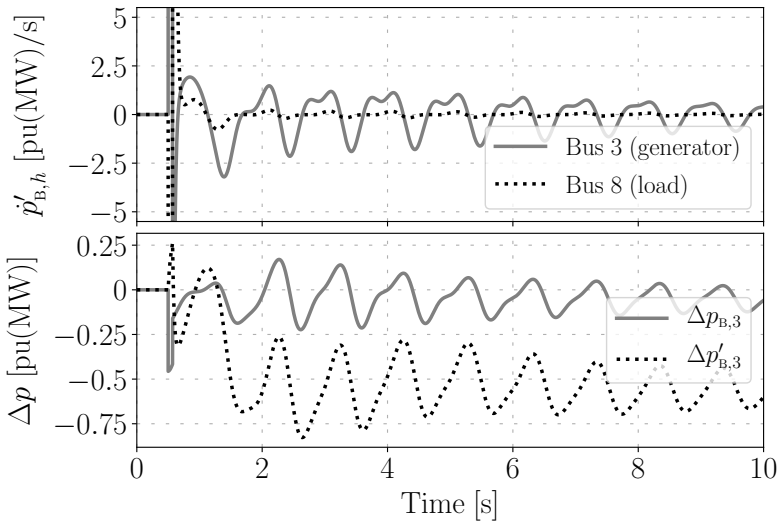

Figure 25 – Use Case FC_D.1 – Top panel: RoCoP at buses 3 and 8. bottom panel: variations of the total and regulating active injected to bus 3

between both trajectories in the plot. After approximately $t = 2$ s, the effect of the inertia diminishes, being replaced by the active power variations due to the PFC. Note that the effect of the inertia does not *vanish* completely after such 2 seconds. The amplitude of $\Delta p'_{\mathrm{B},3}(t)$ is appreciably larger than that of $\Delta p_{\mathrm{B},3}(t)$ during the whole simulation. This indicates that the inertia is naturally contributing during the oscillatory process.

A.3.2 Non-Synchronous Devices

This section discusses the behavior of the RoCoP for non-synchronous devices that do not include noise or whose noise is small enough to be easily decoupled from the effect of the regulation. An in-depth and thorough discussion on the effect of noise in the measured signal on the accuracy of the RoCoP can be found in [33].

In the following, we discuss two examples: 1) passive loads, and 2) ESSs and TCLs.

1) Passive Loads: Loads are equally important with generators for the transient analysis of power systems. For transient stability studies, a passive load connected at the transmission or distribution level is commonly modeled as a constant admittance (see D2.1). This means that during a transient, the power consumption varies quadratically with the voltage magnitude at the load bus. However, such power variations are not due to either intrinsic variations nor a regulation of the load. Instead, they are due to the evolution of the overall system following the contingency. Thus, the RoCoP and consequently the regulating power of passive constant admittances is negligible. This is illustrated in Figure 26, that shows the RoCoP index and power variations of the load at bus 8.

2) ESSs and TCLs: In this example, we compare two families of devices, namely ESSs and TCLs [75, 76]. These devices show substantially different response times with respect to the PFC of SMs: the ESSs is faster (tens-hundreds of milliseconds) and the TCLs is slower (several seconds).

Figure 27 shows the RoCoP, the regulating power estimation and the frequency of the COI when an ESS or a TCL is connected to bus 8. The ESS models a battery storage system [75], and it is connected to bus 8 in antenna through an auxiliary bus, namely bus 8*. The TCL represents 25% of the total load of bus 8. PFC is included in all machines and the contingency considered is again the outage of 20% of the load at bus 5. Both speed and size of the active power variations after the disturbance affect the RoCoP. The difference between power nadirs is less than 50% and the zenith difference of the RoCoP $\dot{p}'_{\mathrm{B},8}(t)$ is about 70%. The ESS has a higher RoCoP than the TCL, and this leads to a significant improvement of the transient response of the system.

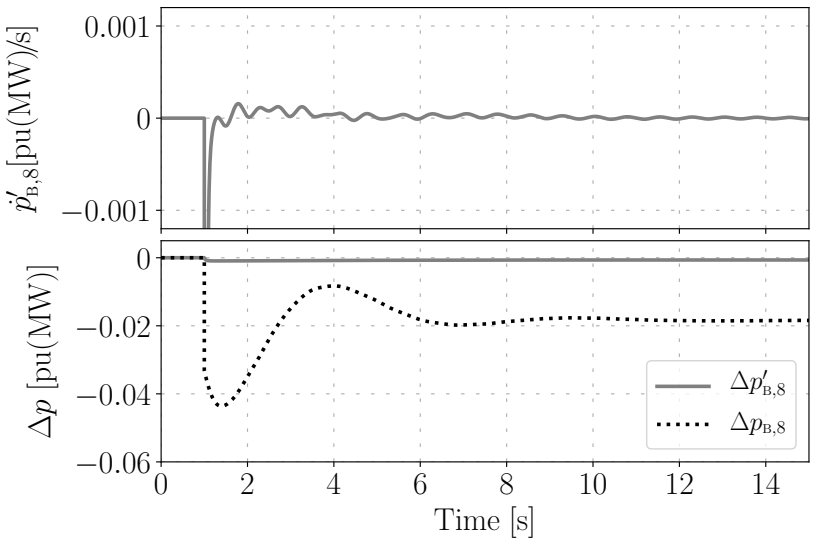

Figure 26 – Use Case FC_D.1 – RoCoP and estimated active power variations of the passive load at bus 8

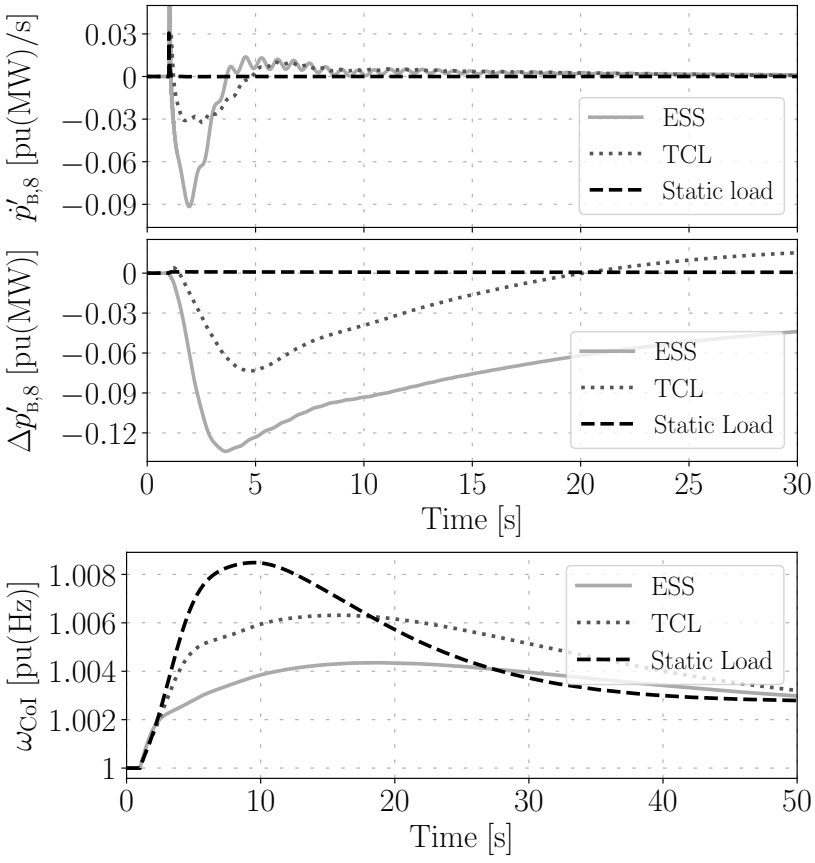

Figure 27 – Use Case FC_D.1 – RoCoP, regulating power variations at bus 8, and frequency of the COI with and without an ESS or a TCL regulating the local frequency

The accuracy of the regulating power estimation is validated next. If the control that regulates the ESS active power output ($p_{\mathrm{ESS}}(t)$) is designed to provide FFR then, in steady-state conditions, $p_{\mathrm{ESS},o} = 0$, thus:

$$\Delta p_{\mathrm{B},8^*}(t) = p_{\mathrm{ESS}}(t) - p_{\mathrm{ESS},o} = p_{\mathrm{ESS}}(t)\ . \tag{A.3}$$

Figure 28 shows that the trajectories of $\Delta p_{\mathrm{B},8^*}(t)$ and $\Delta p'_{\mathrm{B},8^*}(t)$ (the latter calculated with (4.27))

are fairly similar. The small offset (about 4%) that can be observed for $t > 5$ s is due to the fact that (4.15) and, hence, (4.27), do not take into account transmission line losses, nor voltage-driven power variations.

Figure 29 shows the RoCoP and the actual and estimated ESS regulating power with and without a deadband applied to the frequency error signal used as input of the ESS frequency control loop [75]. The inclusion of a 30 mHz deadband (0.0005 pu) introduces a delay in the response of the ESS, which results in a larger amount of power (and thus, of energy) stored by the device. The accuracy of the estimated ESS active power output is not affected by the inclusion of the deadband.

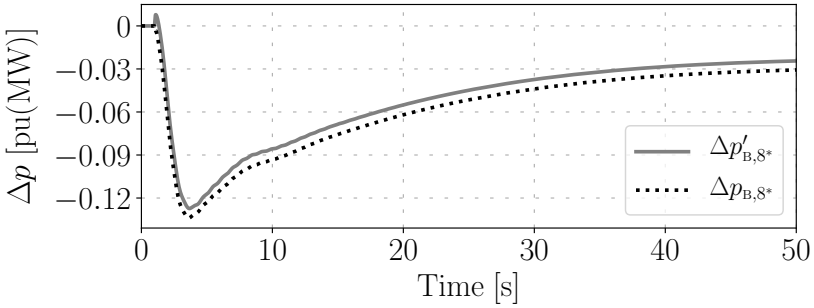

Figure 28 – Use Case FC_D.1 – Variations of regulating power injection and active power output of the ESS regulating the frequency at bus 8*

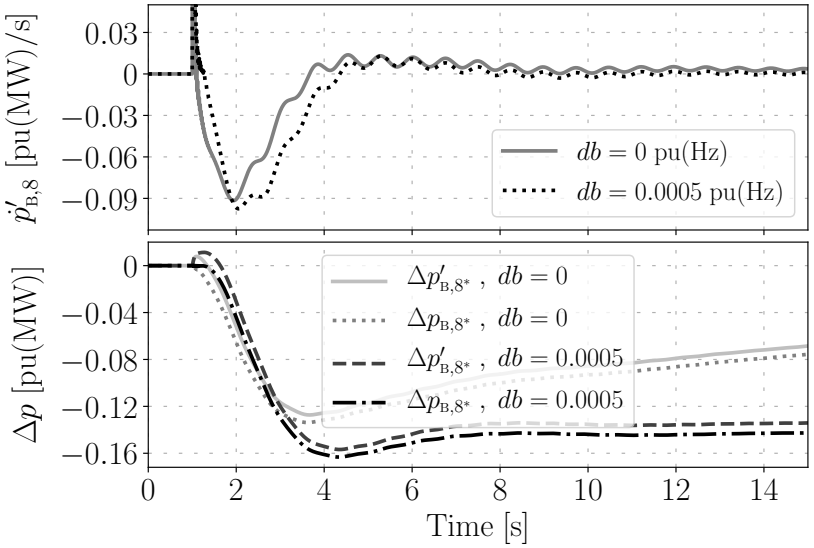

Figure 29 – Use Case FC_D.1 – Regulating power injection at bus 8* and ESS active power output with deadband regulating the local frequency

A.4 Dynamic Inertia Estimation

This section presents simulation results on the dynamic inertia estimation approach presented in Chapter 5. The results are based on Use Case FC_E.1 defined in deliverable D2.1 and the KPIs therein.

A.4.1 Estimation based on RoCoP

A.4.1.1 Synchronous Machines

This example illustrates the expression (5.5) to estimate the equivalent inertia of a device/subsystem. The estimated inertia of the three SMs of the system for the case with only PFC is shown in Figure 30. The estimations are compared with their actual inertia constant, represented by the dashed horizontal lines, and whose values are $M_{\mathrm{G},1} = 47.28$, $M_{\mathrm{G},2} = 12.8$ and $M_{\mathrm{G},3} = 6.02$ MW s/MVA. LPFs with time constant of 1 s have been added to the PLLs utilized to estimate bus frequencies for the three machines to clean the signals from numerical issues due to the sudden jumps of $\dot{p}'_{\mathrm{B},h}(t)$. Results show that, in the first seconds after the contingency, the estimation of the machine inertias is highly accurate. Then, the trajectories drift away from their respective actual values due to the effect of the PFC of the generators.

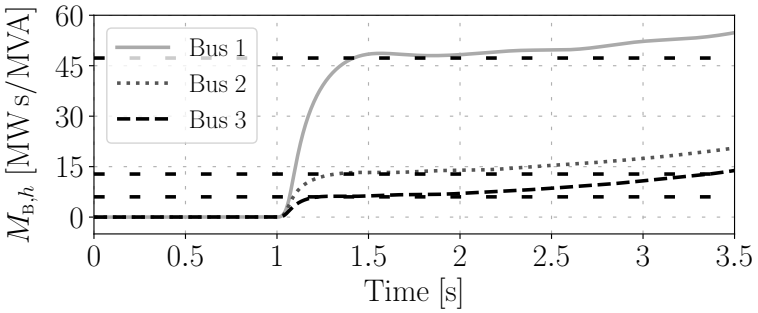

Figure 30 – Use Case FC_E.1 – Estimated inertia of SMs. Dashed lines represent the actual inertia constants

As discussed in the previous example, the inertial response of SMs is dominant during the first instants after a contingency (generally ≤ 1 s). It is in this time window where the proposed technique can be used to estimate the device inertia based exclusively on local power and frequency measurements. This is shown in Figure 31 below, where the absolute and percentage errors of the inertia estimation depicted in Figure 30 are represented.

The estimation errors for the three machines have similar absolute values. This leads to smaller percentage errors for larger machines, which is to be expected as small machines are more affected by the behavior of rest of the system, making more difficult the isolation of the individual impact of such a machine/device. Nevertheless, in the first 600 ms after the estimation fall time (in between 200 and 400 ms depending on the machine), the percentage inertia estimation error is, from the larger to smaller the machine, less than 3%, 8%, 11%, respectively.

Note also that inertia is a fixed parameter of the machine/device, thus being able to estimate its value in the time frame of one second after a contingency will suffice, even though the accuracy of such an estimation is gradually declining with time while the PFC takes part.

A.4.1.2 Non-Synchronous Devices

Finally, the equivalent inertia of both the ESS and the TCL is estimated by means of equation (5.5). Results are displayed in Figure 32.

LPFs are required to filter out the signals from the numerical issues due to the sudden jumps observed in the upper panel of Figure 27 when the loss of load occurs. An equivalent internal reactance

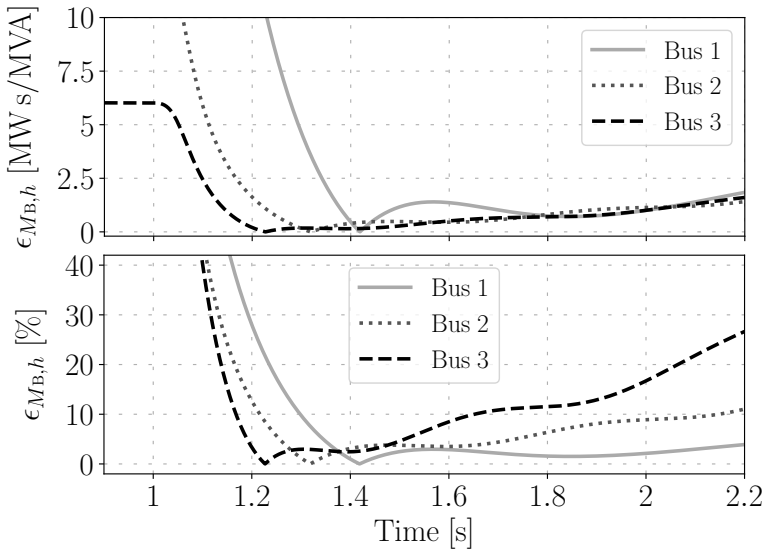

Figure 31 – Use Case FC_E.1 – Absolute and percentage inertia estimation errors of SMs

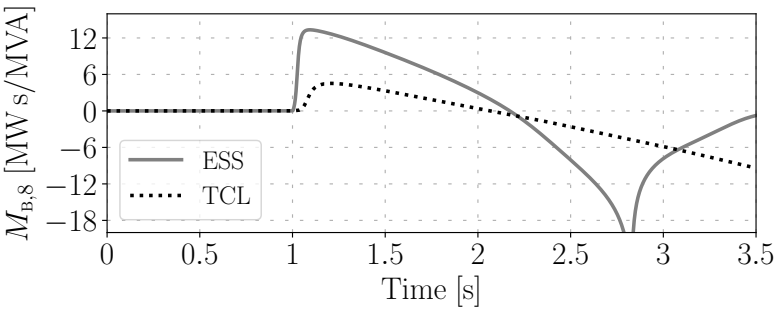

Figure 32 – Use Case FC_E.1 – Estimated inertia of ESS and TCL connected to bus 8

of 1 pu(Ω) is considered in both cases. A time constant for the LPFs of 1 s has been used in the estimation.

As expected, the ESS shows a considerably higher equivalent inertia than the TCL right after the loss of the load. The response of the FFR of the ESS rapidly nullify the denominator of equation (5.5), thus causing the singularity observed at $t \simeq 2.8$ s. The slower response of the TCL delays the occurrence of such a singularity. Note that (5.5) is only valid in the time scale of the typical machine inertial response ($t \lesssim 1$ s), and cannot be used in other time scales (e.g. in steady-state or for long term dynamics).

Note that the singularity of the estimated inertia seen in Figure 32 has no physical meaning. On the other hand, the main information that can be extracted is that while SMs have a constant inertia, non-synchronous devices, although not providing physical inertia, can actually provide during a transient and through their control an equivalent inertia, which, however, is not constant, reaching its maximum in the first instants after a contingency. A noteworthy result of the proposed estimation technique is that it allows quantifying such inertia and thus enables the comparison of different devices and controllers.

A.4.2 Comparison with Improved Estimators

The Use Case FC_E.1 from D2.1 and the KPIs therein are utilized in this section to investigate the performance and accuracy of the proposed on-line inertia and damping estimators.

This section considers and compares three on-line inertia estimators. The estimators are denoted as E0 based on (5.5), E1 based on (5.8) (see Figure 11) and E2 based on (5.12)-(5.13) (see Fig-

ure 13). Three different devices are considered with the following objectives:

1. Verify the accuracy of the proposed estimators to evaluate the inertia constant of SMs;
2. Test the accuracy of the estimators on tracking the constant and time-varying inertia of the grid-forming CIG via a Virtual Synchronous Generators (VSGs) with known inertia;
3. Illustrate the capability of the estimators to evaluate the inertia support from the stochastic renewable source, i.e. the WPP, without and with co-located ESS in grid-following control.

The disturbance considered is a sudden load change and in particular, a 20% increase of the load connected to bus 5, occurring at $t = 1$ s. Moreover, the thresholds $\epsilon_o = \epsilon_p = \epsilon_{\ddot{\omega}} = \epsilon_{\Delta\omega} = 10^{-6}$ are used in Section A.4.2.1 and A.4.2.2. The time step for all time domain simulations is 1 ms. This is also assumed to be the sampling time of the measurements utilized in the proposed estimators.

A.4.2.1 Synchronous Machines

This subsection discusses the performances of the on-line estimators for evaluating the inertia constant of the SM connected to bus 3 (denoted as G3). The actual mechanical starting time and damping coefficient of G3 are $M_{\text{G}} = 6.02$ s and $D_{\text{G}} = 1.0$, respectively. The results discussed in this section are obtained with $T_M = 0.01$ s for E1, and $T_M = 0.001$ s, $T_D = 0.001$ s for E2.

A.4.2.1.1 No Primary Frequency Control

We first assume that G3 has no TG. This is, of course, not realistic, but allows us better illustrating the transient behavior for the estimators. TGs are included in all subsequent simulations. Figure 33 shows the estimated mechanical starting time M^*_{G} of G3 through the three estimators. According to Figure 33, both E1 and E2 can accurately estimate the inertia constant after roughly 80 ms. This period can be decreased with smaller time constants T_M, which, however, can lead to small oscillations.

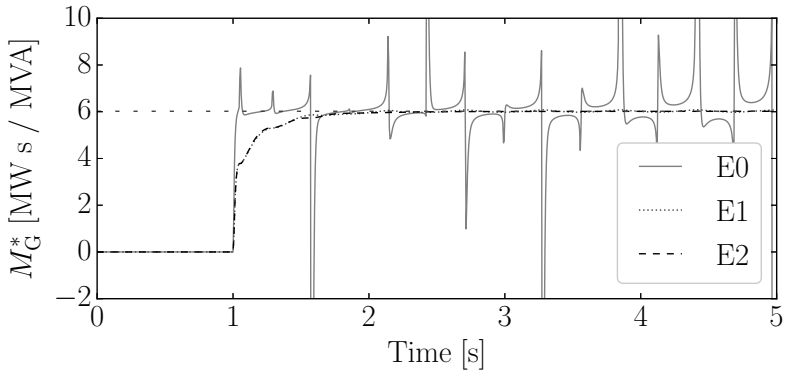

Figure 33 – Use Case FC_E.1 – Estimated inertia of G3 without TG as obtained with E0, E1 and E2

E0 shows a faster response comparing with E1 and E2, but the worst accuracy for introducing spurious spikes. Section 5.4 briefly explains the cause of the spurious spikes, which can be further clarified by Figure 34. As we can see in Figure 34, there is a small phase differences between the nominator $-\dot{\boldsymbol{p}}'^*_{\text{B}}$ and denominator $\ddot{\omega}^*$ of (5.5). It means that they do not cross zero at the same time, and thus when the denominator goes to zero, the numerator is small but no null, hence the large estimation errors and, eventually, the spikes. Given the intrinsic numerical issues of E1, we consider exclusively E1 and E2 in the remainder of the paper.

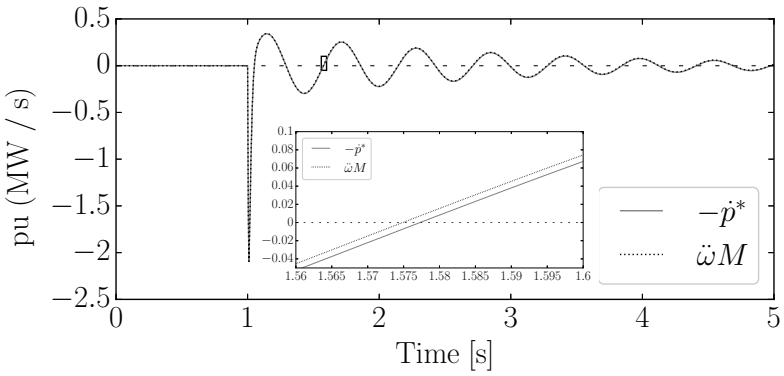

Figure 34 – Use Case FC_E.1 – Dynamic variations of G3 as obtained with E0

A.4.2.1.2 Effect of Primary Frequency Control

Figure 35 shows the estimated inertia of G3 with TG. As it can be seen, E1 and E2 obtain the inertia constant with good accuracy. E2 shows a slightly smaller estimation error than E1.

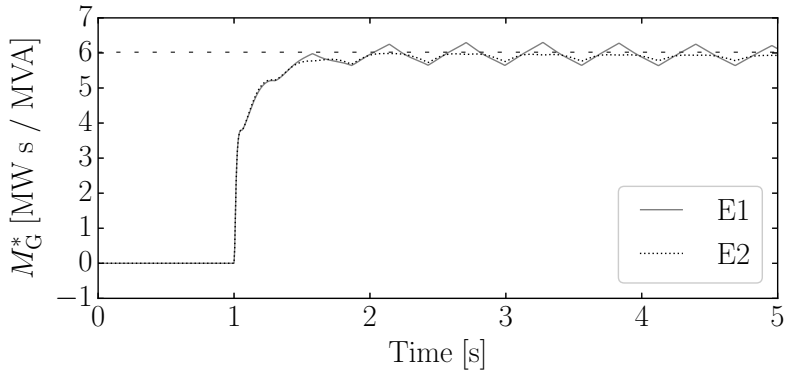

Figure 35 – Use Case FC_E.1 – Estimated inertia of G3 with TG as obtained with E1 and E2

For the sake of example, Figure 36 shows the estimated damping coefficient of G3 with and without TG through the estimator E2. As expected, E2 can accurately estimate the damping D of G3 only if the PFC is not included. This result is consistent with the discussion in Section 5.5. Clearly, PFC is always presented in conventional power plants. But this is not a drawback of the proposed estimation approach as, in practice, the damping of SMs is very small and its estimation is not necessary. Much more relevant is the estimation of the FFR droop gain of non-synchronous devices. This is discussed in Section A.4.2.2.

A.4.2.1.3 Impact of Measurement Noise

This section investigates the robustness of the proposed estimators E1 and E2 against measurement noise. Noise is added to both RoCoP and RoCoF measurements fed into the estimators. The noise is modeled as an Ornstein-Uhlenbeck stochastic process [37]. The standard deviation of the measurement noise are selected according to the expected maximum PMU error at the fundamental frequency [40] and relevant tests for RoCoP measurement [77], namely 0.0001 for RoCoF signal and 0.01 for RoCoP signal. Figure 37 shows the inertia estimated with E1 and E2. Both estimators prove to be robust against measurement noise.

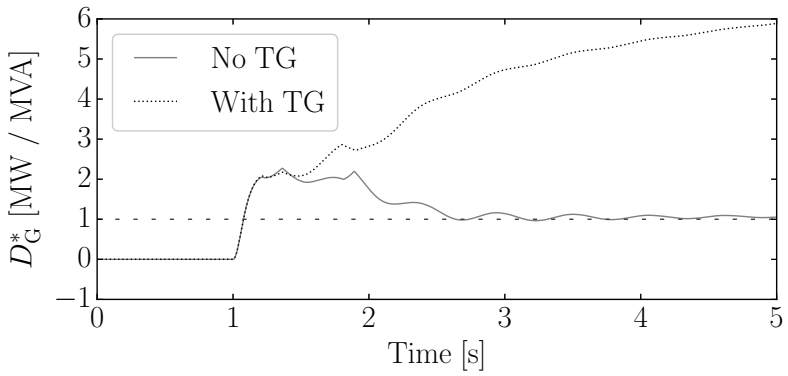

Figure 36 – Use Case FC_E.1 – Estimated damping of G3 with and without TG and without measurement noise as obtained with E2

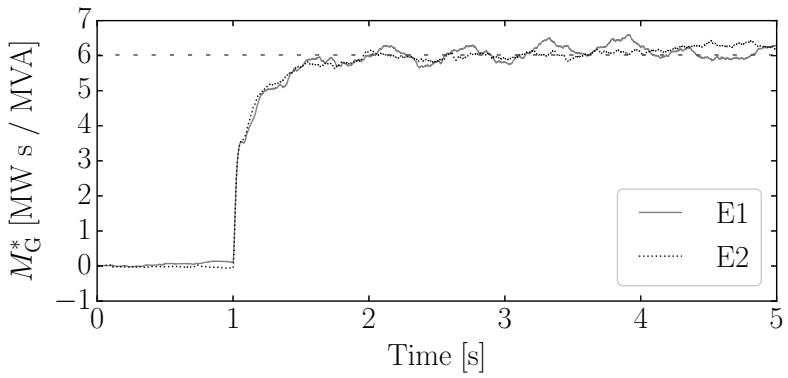

Figure 37 – Use Case FC_E.1 – Inertia of G3 with TG and measurement noise as obtained with E1 and E2

A.4.2.2 Virtual Synchronous Generators

The machine connected to bus 2 of the WSCC system is substituted by a VSG.

The power-electronics-based VSG control is regarded as one of the most effective methods to improve the frequency stability of the low-inertia system in recent years [19]. Since the equivalent inertia of VSGs is imposed by the control of the converter and is thus known *a priori*, the VSG represents a good test to evaluate the accuracy of the inertia estimators proposed in this work.

A.4.2.2.1 VSG With Constant Inertia

We first consider the VSG described in [78]. The inertia and FFR droop gain are considered constant, i.e. $M_{\mathrm{VSG}} = 20$ s and $R_{\mathrm{VSG}} = 20$.

Figure 38 shows the trajectories of the equivalent inertia as obtained with E1 with $T_M = 0.001$ s and E2 with $T_M = 0.001$ s and $T_D = 10^{-4}$ s. E2 obtains the accurate M_{VSG} roughly 60 ms after the contingency, while the estimated inertia of E1 oscillates around the actual value of the inertia. The amplitude of such an oscillation decreases as $\dot{\omega}$ decreases. This is because, in the power electronics device, the droop/damping and the inertia response “pollutes” the inertia estimation as in E1. The additional loop included in E2 for the droop/damping estimation can avoid this issue. Therefore, for the CIG with FFR, E2 performs better than E1. Since the remainder of this section focuses on CIGs, only E2 is considered.

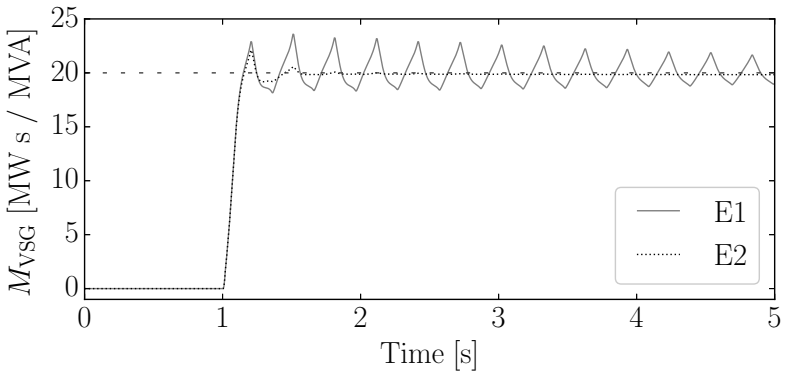

Figure 38 – Use Case FC_E.1 – Estimated inertia of VSG with constant inertia as obtained with E1 and E2

A.4.2.2.2 VSG With Adaptive Inertia

We consider an adaptive VSG, which can tune its inertia with respect to the grid state. The detailed model of the adaptive VSG can be found in [57]. The adaptive VSG has the same droop gain as the VSG with constant inertia discussed above.

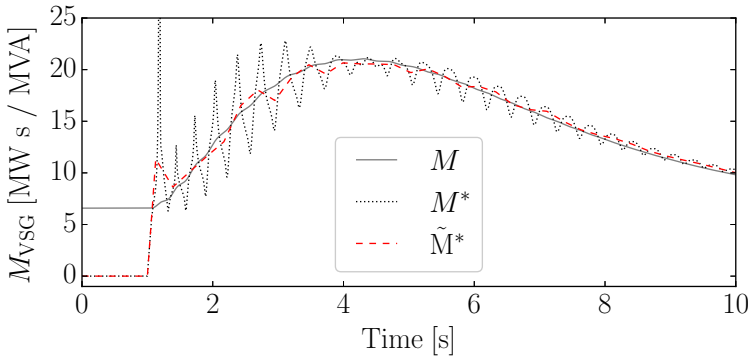

Figure 39 – Use Case FC_E.1 – Estimated inertia of VSG with adaptive inertia as obtained with E2

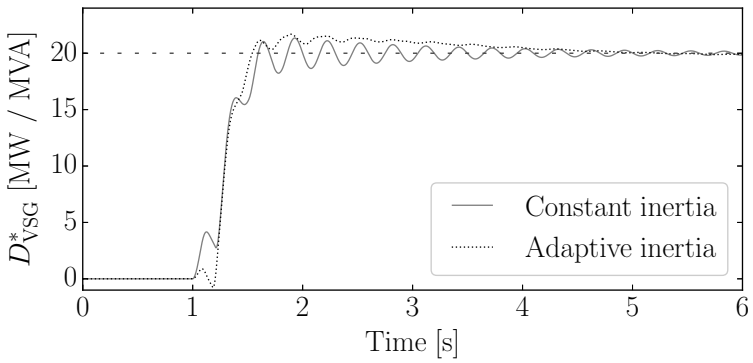

Figure 40 – Use Case FC_E.1 – Estimated droop gain of different VSGs through estimator E2

In order to track the time-varying inertia of the adaptive VSG, we need to decrease the time constant of the estimator. A smaller time constant, however, may lead to spurious oscillations in the estimated result and thus an extra filter is needed. Figure 39 shows the trajectories of the actual inertia M of

the adaptive VSG, the estimated inertia M^* obtained by E2 with $T_M = 5 \cdot 10^{-5}$ s, $T_D = 10^{-4}$ s and the filtered estimated inertia $\tilde{M}^*$. The filter utilized to obtain $\tilde{M}^*$ in Figure 39 is a basic average filter [79] with time constant $T = 0.25$ s. Figure 39 shows that the estimator E2 can accurately track the time-varying inertia with proper parameters and filter.

Figure 40 shows the estimated droop gain of the VSGs with constant and adaptive inertia through E2 with $T_D = 10^{-4}$ s. E2 can accurately estimate the droop gain for these two kinds of VSG. This result is consistent with the discussion in Section 5.5. The oscillations shown in the estimated inertia for adaptive VSG have no impact on the droop gain estimation.

A.4.2.3 Wind Power Plants

This subsection focuses on WPPs modeled as DFIGs. The detailed model of the DFIG can be found in [24]. The wind speed is modeled as an Ornstein-Uhlenbeck stochastic process that fitted with real-world wind speed measurement data [80]. The trajectories of the wind speed obtained from 500 Monte Carlo simulations. In all the figures shown in this section, μ and σ represent the mean and standard deviation of the simulated time series.

All the trajectories of the estimated inertia presented in this subsection are obtained through the estimator E2 with $T_M = 0.001$ s and $T_D = 0.001$ s. In order to depress the impact of the stochastic wind, we set $\epsilon_{\ddot{\omega}} = 2 \cdot 10^{-4}$ and $\epsilon_{\Delta\omega} = 0.1$.

The machine connected to bus 2 of the WSCC system is substituted by a WPP.

A.4.2.3.1 WPP Without ESS

We first consider the case of the DFIG without ESS. Figure 41 shows the trajectories of the output active power of the WPP following the sudden load increase. The WPP has limited response to the contingency. The active power of the WPP varies following the dynamics of the wind speed, while the mean remains the same before and after the occurrence of the contingency. Accordingly, the estimated inertia of the WPP are within the small range $M^*_{\text{WPP}} \in [-0.28, 0.1]$ and the mean is almost zero, according to Figure 42. Figure 42 also shows that the inertia estimation is not biased by the stochastic wind dynamics resulted before the contingency. The values of $\epsilon_{\ddot{\omega}}$ and $\epsilon_{\Delta\omega}$, therefore, are adequate.

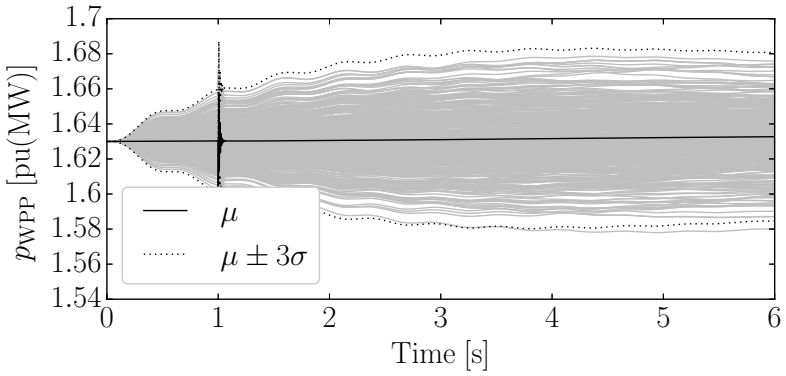

Figure 41 – Use Case FC_E.1 – Output active power of the WPP without ESS

As expected, the results shown in Figures 41 and 42 lead to conclude that the WPP without frequency control nor ESS does not provide any significant inertia support to the system.

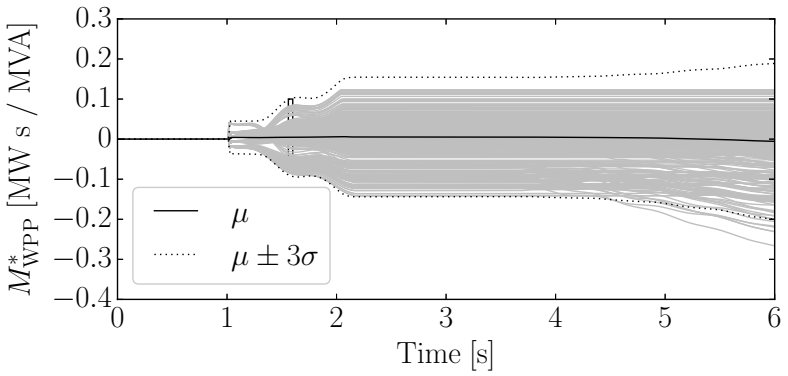

Figure 42 – Use Case FC_E.1 – Estimated inertia of the WPP without ESS

A.4.2.3.2 WPP with ESS

We consider the DFIG coupled with an ESS. The ESS is modeled as a Grid-Following Converter (GFC) with RoCoF control. The detailed model of the GFC can be found in [81]. Due to the short-term analysis, the storage limits of the ESS are not considered. The gain of the RoCoF control in the ESS is 40.

Figure 43 shows the trajectories of the output active power of the DFIG with the ESS obtained from 500 Monte Carlo simulations. The active power of the WPP with ESS increases after the occurrence of the contingency, while its magnitude vary slightly depending on the stochastic wind speed.

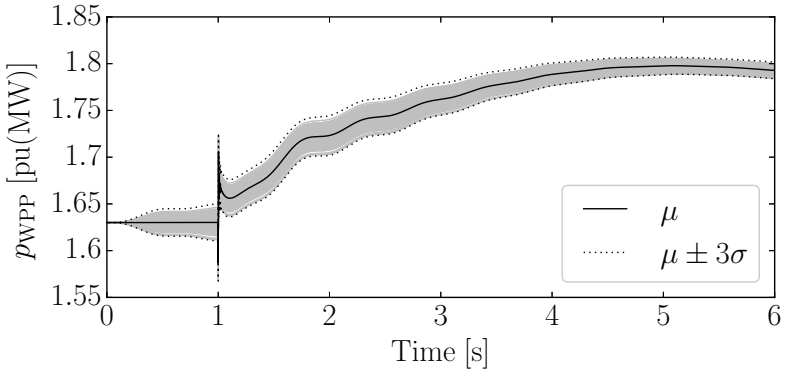

Figure 43 – Use Case FC_E.1 – Output active power of the WPP with ESS

Figure 44 shows the estimated inertia of the WPP with ESS through the on-line inertia estimator E2 in 500 tests. Consistently with the uncertain active power injection shown in Figure 43, the equivalent inertia provided by the WPP varies within the range $M^*_{\mathrm{WPP}} \in [33.1, 45.8]$ according to Figure 44. The average value of the WPP inertia is 40 s, which is consistent with the RoCoF control gain. These results indicate that the WPP can provide an inertial response through the RoCoF control of its ESS.

A.4.2.3.3 SM in System With High Wind Penetration

We consider again the system discussed in Section A.4.2.3.2 but, in this case, we focus on the estimation of the inertia of the synchronous generator G3 via estimator E2. Since the system includes a stochastic energy source, the thresholds are $\epsilon_{\ddot{\omega}} = 2 \cdot 10^{-4}$ and $\epsilon_{\Delta\omega} = 0.1$, and the time constants are $T_M = T_D = 0.001$ s.

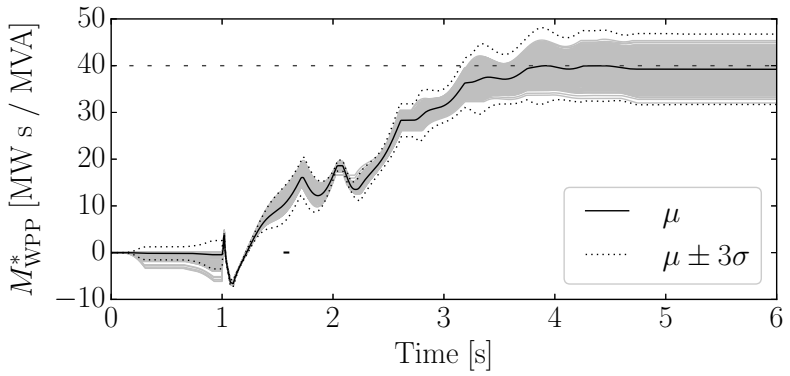

Figure 44 – Use Case FC_E.1 – Estimated inertia of the WPP with ESS

Figure 45 shows the estimated inertia of G3 in the revised WSCC system with high wind penetration and FFR energy storage through the on-line inertia estimator E2 obtained with 500 simulations. E2 shows a satisfactory accuracy, even though small fluctuations are introduced compared to the results discussed in Section A.4.2.1. In the vast majority of Monte Carlo realizations, the thresholds avoid to trigger the inertia estimation before the occurrence of the contingency. In general, thus, and as shown in Figure 45, the accuracy of inertia estimation following the contingency is not affected by noise. These results also demonstrate that E2 is able to obtain an accurate estimation of the inertia of a specific device even if the system include other devices with faster dynamics and controllers.

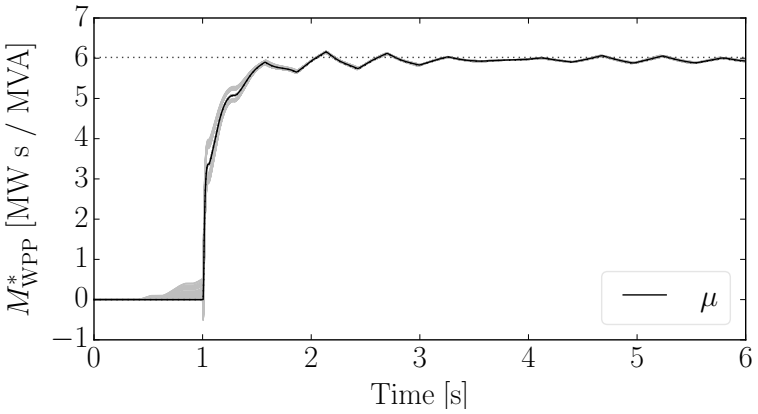

Figure 45 – Use Case FC_E.1 – Estimated inertia of G3 with inclusion of WPP and ESS